Characteristics of deep crustal seismic anisotropy from a compilation of rock elasticity tensors and their expression in receiver functions

Sarah J. Brownlee[1], Vera Schulte-Pelkum[2], Anissha Raju[3], Kevin Mahan[3], Cailey Condit[3], and Omero Felipe Orlandini[3]

[1]Department of Geology, Wayne State University, Detroit, Michigan, USA, [2]Cooperative Institute for Research in Environmental Sciences and Department of Geological Sciences, University of Colorado Boulder, Boulder, Colorado, USA, [3]Department of Geological Sciences, University of Colorado Boulder, Boulder, Colorado, USA

Abstract Rocks in the continental crust are long lived and have the potential to record a wide span of tectonic history in rock fabric. Mapping rock fabric in situ at depth requires the application of seismic methods. Below depths of microcrack closure seismic anisotropy presumably reflects the shape and crystallographic preferred orientations influenced by deformation processes. Interpretation of seismic observables relevant for anisotropy requires assumptions on the symmetry and orientation of the bulk elastic tensor. We compare commonly made assumptions against a compilation of 95 bulk elastic tensors from laboratory measurements, including electron backscatter diffraction and ultrasound, on crustal rocks. The majority of samples developed fabric at pressures corresponding to middle to lower crustal condition. Tensor symmetry is a function of mineral modal composition, with mica-rich samples trending toward hexagonal symmetry, amphibole-rich samples trending toward an increased orthorhombic symmetry component, and quartz-feldspar-rich samples showing a larger component of lower symmetries. Seventy-seven percent of samples have a best fit hexagonal tensor with slow-axis symmetry, as opposed to mantle deformation fabric that usually has fast-axis symmetry. The best fit hexagonal approximation for crustal tensors is not elliptical but deviates systematically from elliptical symmetry with increasing anisotropy, an observation that affects the magnitude and orientation of anisotropy inferred from receiver function and surface wave observations. We present empirical linear relationships between anisotropy and ellipticity for crustal rocks. The maximum out-of-plane conversion amplitudes in receiver functions scale linearly with degree of anisotropy for nonelliptical symmetry. The elliptical assumption results in a bias of up to 1.4 times true anisotropy.

1. Introduction

Our understanding of the structure of Earth, from core to crust, is derived mainly from seismic observations. Most of these observations are collected on continents because that is where the densest arrays of seismometers can be placed. Thus, our observations of the deeper parts of the Earth are often viewed through the window of the continents, making it critical to understand the structure and composition of the continental crust and how it affects seismic and other geophysical observations. In principle, the longevity of continental crust also allows reconstruction of tectonic processes over a long time range.

Recent developments in methods for observing seismic anisotropy have made detection of crustal anisotropy more common. These studies have also demonstrated that crustal anisotropy is more complex than mantle anisotropy and can be strong enough to have an effect on mantle observations if not accounted for. Seismic anisotropy in the crust comes from three main sources: (1) oriented cracks and microcracks (most important in shallow crust) [e.g., *Crampin*, 1981; *Nishizawa*, 1982; *Crampin*, 1994], (2) crystallographic preferred orientation (CPO) of minerals [e.g., *Silver and Chan*, 1991; *Savage*, 1999], and (3) compositional layering [e.g., *Backus*, 1965]. Our ability to interpret crustal anisotropy, in particular in the middle and lower parts of the crust, relies on measurements of the elastic properties, i.e., elastic tensors (intrinsic anisotropy), of crustal rocks and an understanding of the effects of layering and larger-scale structure (extrinsic anisotropy).

Elastic tensors of rocks can be constructed in two ways: (1) physically measuring the acoustic velocities in different directions through a sample, and (2) measuring the CPO of constituent minerals in a sample and calculating an elastic tensor based on a combination of single-crystal elastic tensors rotated and averaged to reflect each mineral CPO and the volume proportion of minerals in the sample. Some CPO-based

Table 1. Sources, Methods, and Sample Localities for the Elastic Tensors in the Compilation

Source	Method	Locality	# of tensors
Tatham et al. [2008]	EBSD	Upper Badcall shear zone, Scotland	8
Ward et al. [2012]	EBSD	Wyoming, USA	3
Brownlee et al. [2011]	EBSD	Papua New Guinea	6
Erdman et al. [2013]	EBSD	Basin and Range, USA	25
Brownlee, unpublished data	EBSD	Southern California and North Carolina	28
Weiss et al. [1999]	U stage	Italy	8
Barberini et al. [2007]	U stage	Italy	2
Khazanehdari et al. [1998]	X-ray	Italy	1
Valcke et al. [2006]	X-ray	North Sea	3
Ji et al. [2013]	Ultrasound	China and Saskatchewan, Canada	6
Takanashi et al. [2001]	Ultrasound	Japan	4
Rasolofosaon et al. [2000]	Ultrasound	Germany	1

methods such as asymptotic expansion homogenization also consider the compositional textures and structure in the sample, such as banding.

A number of studies over the last 30 years or so have reported elastic tensors for crustal rocks using acoustic and/or CPO-based measurements. We have compiled reported elastic tensors from published studies and in some cases directly from investigators for publications that used complete elastic tensors but did not include them in the published results or publications that are still in preparation. Analysis of these tensors, including rock type and composition, provides a framework from which interpretations of crustal anisotropy can be based. These tensors are derived from the rocks and do not depend on assumptions of simplified symmetry, so they also provide a basis for more realistic symmetry assumptions, as well as guidelines for situations in which simplified symmetries are not good approximations.

We report a first-cut analysis of the tensor compilation focusing on the magnitude of anisotropy, the symmetry components, and how these properties are related to rock type and composition. The analysis is preliminary because the compilation will continue to grow as more studies measure the elastic tensors of crustal rocks, but this first cut reveals patterns and trends that will be immediately useful for improving seismic inversion methods and interpretations of crustal anisotropy. We also perform seismic forward modeling to investigate what the trends observed in our compilation imply for the interpretation of seismic observations.

2. Description of Tensor Compilation

2.1. Rock Composition and Deformation Conditions

The current compilation includes 95 tensors covering a wide variety of crustal rock types (sample locations are listed in Table 1, and shown in Figure 1c). The majority of the tensors are from gneisses and schists deformed at middle and lower crustal conditions (~300–900°C and 4–9 kbar). The compilation includes some highly deformed mylonitic rocks, as well as some igneous intrusives with little deformation. Other rock types, such as sandstone, quartzite, calc-silicates, marbles, and metavolcanics, are also represented. The mineral proportions range from >90% quartz to >70% amphibole to 90% dolomite and calcite. SiO_2 contents range from ~5–90%, such that the compilation covers the wide variety of compositions that might be found in the middle and lower crust. The expected middle and lower crustal rock types and possible compositions are all represented, but statistically the compilation is not representative of the middle and lower crust; for instance, there is only one tensor from an anhydrous granulite. Nonetheless, most of the tensors are from rocks expected to be present within the deeper portion of the crustal column. The tensor compilation comprises 44% quartzofeldspathic rocks with igneous or supracrustal protoliths (28% gneisses and 16% plutonic rocks with no gneissic banding); 15% mica schists; 22% amphibolites; 10% calc-silicates; and 3% or less sandstone, granofels, quartzite, mafic eclogite, and granulite (Figure 1a). When characterized based on metamorphic temperatures for fabric development, the compilation is approximately evenly split into low-grade (30% at ~300–500°C), midgrade (40% at 500–700°C), and high-grade (30% at 700–900°C) samples. There are an additional six tensors from ultrahigh-pressure rocks. The compilation is naturally biased toward visibly deformed rocks, since those tend to be the subject of studies that incorporate texture analysis and therefore may be biased toward higher anisotropy compared to average bulk continental crust. However, the trends relating mineralogy and rock type to anisotropy and symmetry are not expected to be significantly affected by this bias.
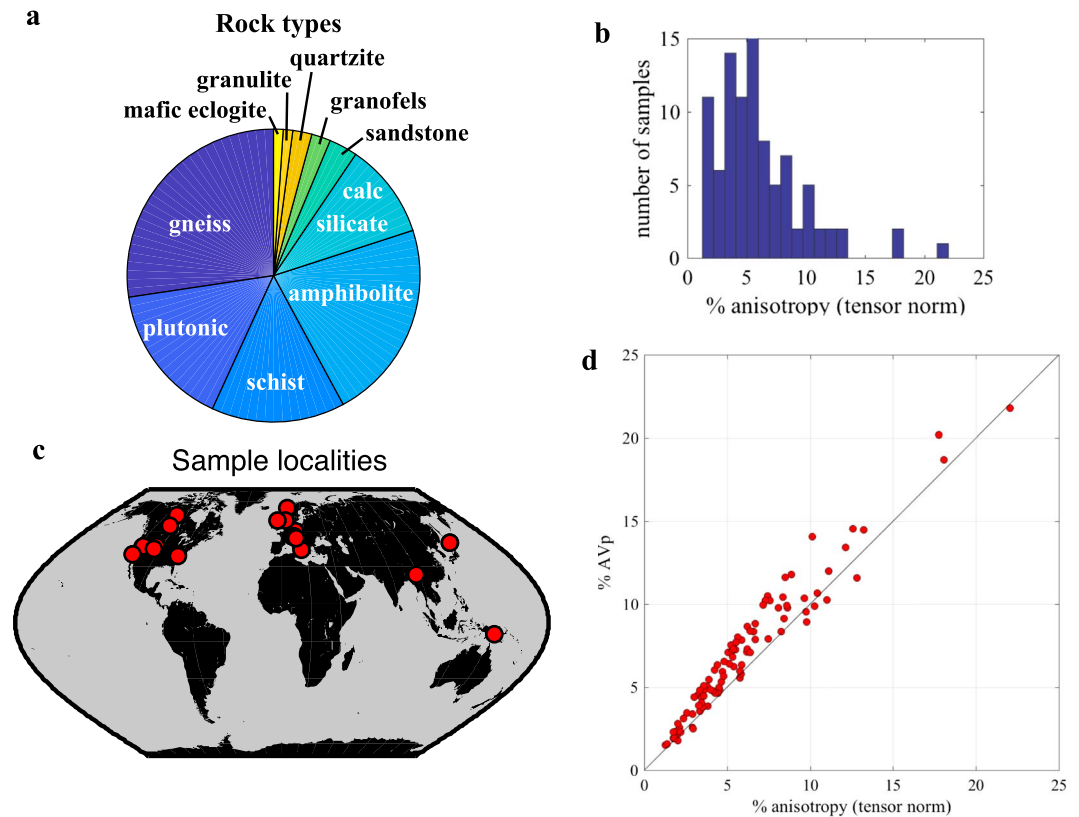
Figure 1. (a) Breakdown of the samples in the elastic tensor compilation by rock type. (b) Histogram of the strength of anisotropy of the samples in the compilation, with anisotropy strength based on fraction of the total tensor norm. (c) Location map for the samples in the tensor compilation. (d) Scatterplot of tensor norm anisotropy versus Vp anisotropy, AVp, which is the difference between maximum and minimum Vp as a percentage of the mean Vp (further defined in section 3.2). Diagonal line shows a ratio of 1, where samples would fall if the two measures of anisotropy coincide.

2.2. Methods of Elastic Tensor Determination

The compilation includes tensors determined by three different methods (Table 1). The majority are from mineral CPO-based calculations (electron backscatter diffraction (EBSD) at 74%, X-ray texture goniometry at 4%, and universal stage at 11%). The remaining 11% are based on ultrasonic or pulse transmission acoustic velocity measurements. There are some important considerations when comparing results from different methods. Acoustic velocity measurements determine the velocity in particular directions and then fit an elastic tensor to the data. Most methods use core samples taken in the directions of the principal rock fabric axes: Z—perpendicular to foliation, X—parallel to lineation, and Y—perpendicular to X and Z (perpendicular to lineation and parallel to foliation). A required assumption for fitting a tensor to the measured velocities is that the true maximum and minimum velocities have been measured, which may not be the case when only three or even six cores are used. Inverting individual core velocities for an elastic tensor also requires assuming a simplified symmetry. Some laboratories use spherical samples, which allows the velocity in many different directions to be measured on the same sample (e.g., *Rasolofosaon et al.* [2000] and a sample in *Weiss et al.* [1999]), an advantage over core samples because there is no requirement of simplified symmetry. We use ultrasound measurements that were conducted under confining pressures sufficient for crack closure.

The CPO-based measurements use determinations of mineral CPO in conjunction with single-crystal elastic constants for the constituent minerals in the sample to calculate an average elastic tensor for the rock. The most common method for determining mineral CPO is electron backscatter diffraction (EBSD). EBSD produces a diffraction pattern in a scanning electron microscope by sending an electron beam toward a highly polished surface at an incident angle of ~20°. The electrons are diffracted by the crystal lattice as the beam enters and exits the surface of the material, producing a pattern that is characteristic of the mineral and its crystallographic orientation. The distribution of crystallographic orientations in a sample can be

determined by measuring the orientations of a large number of grains of each mineral in the sample. Several EBSD-based studies compare velocity results to ultrasound measurements on the same samples, and vice versa, and find that they are typically within ~5% of one another for the velocities in the principal directions [*Barruol and Kern*, 1996; *Weiss et al.*, 1999; *Brownlee et al.*, 2011; *Erdman et al.*, 2013].

Another method for determining mineral CPO is X-ray texture goniometry (XTG). This method also produces diffraction patterns but from a larger volume of material and for finer-grained material. The pattern produced is a function of the distribution of orientations in the material. Both EBSD and XTG can produce aggregate elastic tensors for the rock without enforcing any symmetry assumptions and without assuming that the principal velocity directions will match the principal fabric axes.

Predating the automated CPO determination via EBSD or XTG is the universal stage. Universal stage methods utilize a multiaxis stage on a standard petrographic microscope that has five axes of rotation, which allows determination of the orientation of the optic axis of the minerals present in the sample. This method is considerably more time intensive than EBSD methods because it cannot be automated, and thus, most universal stage CPO determinations stop at ~300–500 orientation determinations per sample. Counting statistics on random samples of 200 grains from a particular orientation distribution are generally within uncertainty of the full distribution, so universal stage determinations are likely to be as representative of the true orientation distribution as EBSD determinations from the same area of a thin section. The uncertainty of individual orientation measurements is highly dependent on the experience of the user for both U stage and EBSD. The main advantages of EBSD over U stage are the ability to cover large areas in a short period of time and a higher spatial resolution (submicron for EBSD versus ~30 μm for U stage).

There are advantages and disadvantages to both acoustic velocity methods and CPO-based methods. An advantage of CPO-based methods is that secondary effects such as cracks and late alteration features that may not have been present when the targeted rock fabric developed can be avoided. An advantage of acoustic velocity methods is that measurements are typically made at various confining pressures, such that once cracks have closed, it is possible to determine the partial derivatives of velocity with respect to pressure for the aggregate. Acoustic velocity determinations are, however, generally restricted to a limited number of directions. Acoustic velocity measurements are also significantly more labor intensive and cost intensive than CPO-based methods, particularly those employing EBSD. X-ray methods have an advantage over EBSD in that they completely characterize the orientation distribution in a volume of material, but X-ray methods are generally restricted to fine-grained materials. One of the main limitations to CPO-based techniques is that the calculation of the aggregate elastic tensor is limited by the availability and accuracy of single-crystal elastic tensors for constituent minerals. For most crustal minerals, the single-crystal elastic tensors are only measured at standard temperature and pressure conditions (STP). The majority of the tensors in this compilation are thus reported at STP. For rocks of known composition, the STP tensors can be scaled to crustal pressure and temperature conditions using an isotropic scaling based on calculated partial derivatives of bulk and shear moduli for the rock composition [e.g., *Hacker et al.*, 2003]. Isotropic scaling will not account for the effects of particular elastic constants having different partial derivatives with respect to pressure and temperature, but it does allow for a more direct comparison to measured seismic velocities. The discussion in this paper is mainly concerned with trends in the magnitude and symmetry of seismic anisotropy related to rock type and mineralogy. Since the exact behavior of elastic tensors with pressure *and* temperature is not well characterized, even for single minerals, we will focus on analyzing the trends we observe using the tensors as reported. We note a need for additional determinations of single-crystal elastic constants and their pressure and temperature partial derivatives in order to calculate more accurate elastic tensors for realistic crustal conditions than what is possible currently.

3. Characteristics of Tensor Compilation

3.1. Decomposition Into Symmetry Components

We use the tensor decomposition introduced by *Browaeys and Chevrot* [2004] to determine to what extent the full sample tensors are described by isotropic, hexagonal, orthorhombic, or lower symmetries. An isotropic elastic medium is described by two independent elastic constants and supports compressional (*P*) and shear (*S*) waves with spherical phase velocity surfaces (the surface formed by a wavefront around a source point in the medium at a given point in time). In an anisotropic medium, the elastic waves cease to be

purely compressional or shear waves [*Aki and Richards*, 1980; *Babuska and Cara*, 1991], but for weak anisotropy (approximately to 10% [*Park and Levin*, 2016]), they can be described as a quasi-compressional (qP) wave and a slow and a fast S wave with orthogonal polarizations. In an anisotropic medium with hexagonal symmetry, also known as transverse isotropy, the elastic tensor has five independent elastic constants, and the qP phase velocity surface has one unique symmetry axis with a circular cross section perpendicular to it. For the orthorhombic case (nine independent elastic constants), the qP velocity surface is an ellipsoid with three unique and orthogonal axes.

The symmetry decomposition method [*Browaeys and Chevrot*, 2004] involves projecting a vectorized version of the full elastic tensor with 21 independent components, corresponding to the lowest-order (triclinic) symmetry, onto orthogonal vectors corresponding to the different symmetry classes. This is done in order from highest to lowest-order symmetry, removing the portion of the tensor that fits into each symmetry class. Initially, the isotropic component is removed, followed sequentially by hexagonal, tetragonal, orthorhombic, and monoclinic components. The remaining tensor after all symmetry components are removed is the triclinic component. This method does not consider some possible symmetry classes, such as trigonal, so the triclinic component could yet contain some symmetry, but while these components are present in minerals, we do not expect aggregate rock tensors to contain significant proportions of other symmetry classes. The extent to which the full tensor is represented by each symmetry class is quantified by the norm of each symmetry component vector divided by the full tensor norm, i.e., the percentage of the full tensor norm.

3.2. Magnitude of Anisotropy and Rock Types

The tensors in the compilation have a range of 1% to 22% anisotropy as measured by the percent of the tensor norm that is not isotropic, with a median value of just over 5% (Figure 1b). A different measure of anisotropy in standard use [*Birch*, 1960; *Mainprice*, 1990] is based solely on the difference between the maximum and minimum velocity, e.g., for compressional velocity, $AVp = (Vp_{max} - Vp_{min})/Vp_{avg}$, where $Vp_{avg} = 0.5 \times (Vp_{max} + Vp_{min})$. Tensor norm anisotropy and AVp of individual tensors in our compilation show close agreement for most samples, with AVp slightly higher than tensor anisotropy by a factor of 1.18 in median (Figure 1d).

3.3. Hexagonal Symmetry: Fast Versus Slow Axis, Off-Axis Behavior, and Ellipticity

Hexagonal symmetry, as the simplest anisotropic case, is a typical assumption made in seismological studies of anisotropy. Common special cases are radial anisotropy (vertical symmetry axis), targeted in surface wave studies using the Love-Rayleigh discrepancy [e.g., *Shapiro et al.*, 2004; *Moschetti et al.*, 2010; *Xie et al.*, 2013], and azimuthal anisotropy (horizontal symmetry axis), addressed in SKS splitting and Rayleigh wave anisotropy studies.

Hexagonal anisotropy or transverse isotropy has been termed "melon-shaped anisotropy" in the fast-axis case and "pumpkin-shaped anisotropy" in the slow-axis case [*Levin and Park*, 1998]. Mantle anisotropy is reasonably well approximated by fast-axis hexagonal symmetry [*Becker et al.*, 2006]. Crustal slow- or fast-axis anisotropy inferred from receiver function azimuthal conversion amplitude variations is variously inverted for or chosen via forward modeling [*Frederiksen et al.*, 2003; *Zandt et al.*, 2003; *Sherrington et al.*, 2004; *Audet*, 2015; *Liu et al.*, 2015; *Liu and Park*, 2017] or assumed to be slow-axis hexagonal symmetry a priori [*Weiss et al.*, 1999; *Vergne et al.*, 2003; *Ozacar and Zandt*, 2004, 2009; *Porter et al.*, 2011; *Olugboji and Park*, 2016], especially when mica is considered the dominant crystallographically aligned mineral [*Shapiro et al.*, 2004]. Amphibole anisotropy can produce fast-axis symmetry and is also invoked [*Sun et al.*, 2012], and fast-axis symmetry in the crust may be assumed in receiver function inversions [*Bianchi et al.*, 2015]. Most receiver function studies that target splitting of the Moho Ps converted phase [*McNamara and Owens*, 1993; *Peng and Humphreys*, 1997; *Nagaya et al.*, 2008; *Nagaya et al.*, 2011; *Liu and Niu*, 2012; *Sun et al.*, 2012; *Shen et al.*, 2015; *Sun et al.*, 2015; *Kong et al.*, 2016; *Niu et al.*, 2016; *Wang et al.*, 2016] solve for a fast horizontal axis orientation, as is standard in shear wave splitting studies. Surface wave studies targeting crustal radial anisotropy (vertical symmetry axis) find dominantly $V_{SH} > V_{SV}$ [*Moschetti et al.*, 2010; *Xie et al.*, 2013] indicating slow-axis symmetry. Our crustal compilation shows 77% slow-axis symmetry in the best fit hexagonal approximation and only 23% fast-axis symmetry.
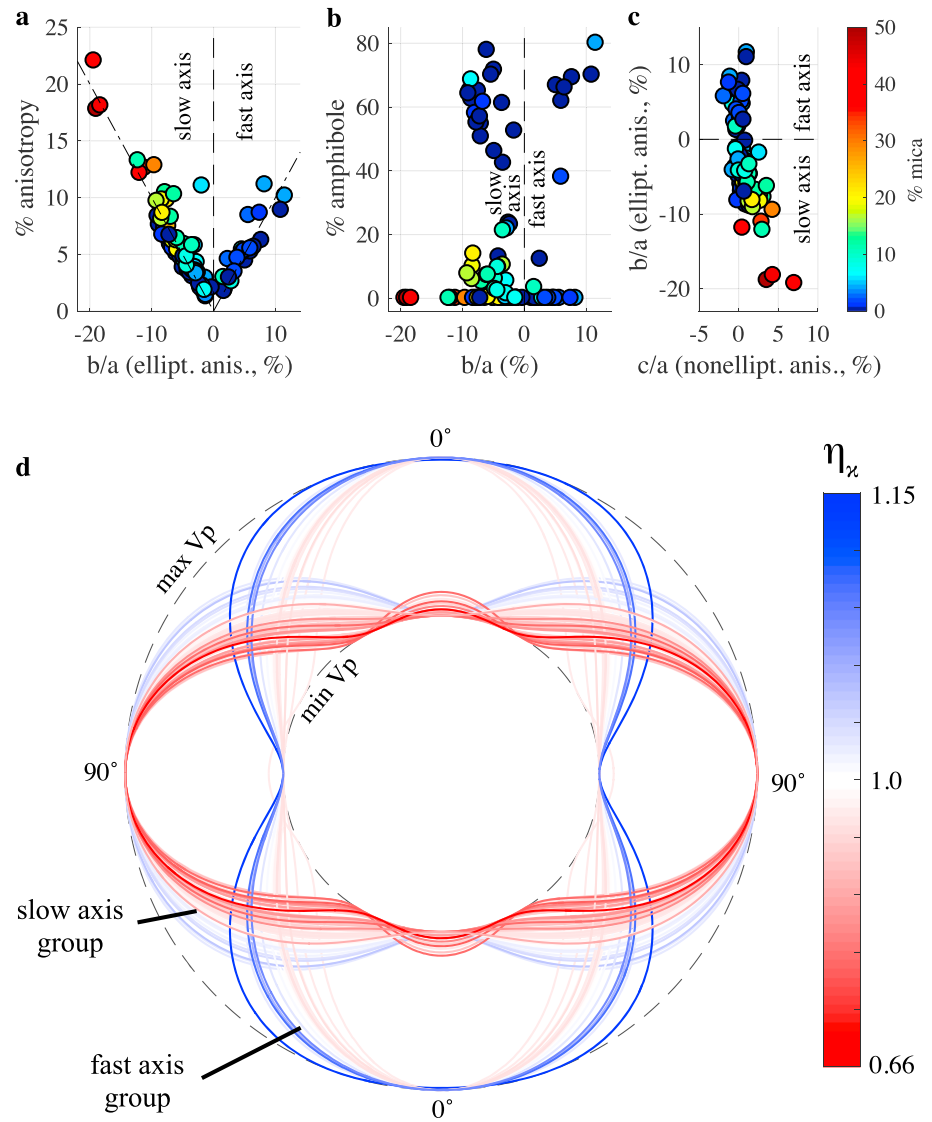
Figure 2. (a) Scatterplot for all samples in the compilation showing percent tensor anisotropy as a function of Backus coefficient *b* (corresponding to elliptical anisotropy, shown in percent) of the best fit hexagonal tensor, normalized by Backus coefficient *a* (corresponding to average Vp). Color fill shows percentage of mica (same color scale for Figures 2a–2c, shown on right). Negative values of normalized *b* correspond to slow-axis hexagonal symmetry, positive values to fast axis. Vertical dashed line separates slow- and fast-axis domains. Diagonal dash-dotted lines show where total tensor anisotropy has the same magnitude as the elliptical hexagonal anisotropy (*b/a*). (b) Same as Figure 2a, except with vertical axis showing percent amphibole. (c) Backus parameter *c*, describing the deviation from elliptical anisotropy, as a function of elliptical anisotropy. Parameter *c* = 0 for the elliptical case. Parameter *c* increases with increasing total anisotropy and increasing elliptical anisotropy, *b*, particularly for slow-axis symmetry, mica-bearing samples. (d) Slice through Vp phase velocity surfaces for all samples in the compilation. The symmetry axis is vertical, and the symmetry plane horizontal. Velocities were scaled to a common minimum (min Vp) and maximum (max Vp) to emphasize the shape of the phase velocity surface. Color shows deviation from the elliptical case.

Different notation conventions exist for the five independent elastic parameters in the hexagonal case (Love coefficients [*Love*, 1944]; Backus coefficients [*Backus*, 1965; *Crampin*, 1977; *Park*, 1996]; and Thomsen coefficients [*Thomsen*, 1986]). We provide conversions between each set in Appendix A. Figure 2a shows compositional trends and trends with strength of anisotropy of the two hexagonal symmetry groups. We display the Backus coefficient *b*, representing azimuthal variation of hexagonal anisotropy, normalized by Backus coefficient *a*, representing average Vp [*Backus*, 1965], since this parameter indicates slow (*b* < 0) or fast (*b* > 0) axis symmetry. All mica-rich samples fall in the slow-axis category, which also shows samples with stronger

anisotropy, both by total anisotropy (vertical axis) and by azimuthal variation of the hexagonal approximation (horizontal axis). The two measures of anisotropy scale similarly for most samples, with a few outliers. A scatterplot with amphibole content, azimuthal anisotropy b/a, and mica content (Figure 2b) shows that while mica-rich samples always show slow-axis symmetry, amphibolites can fall into either the slow- or fast-axis symmetry group. *Ji et al.* [2013, 2015] ascribed differences in amphibolite symmetry to deformation type. Many of the publications our samples were compiled from do not provide sufficient fabric information to investigate such relationships, and we encourage publication of *J* or *M* [*Skemer et al.*, 2005] indices along with the full elastic tensor.

A second assumption made in seismic studies invoking hexagonal symmetry, with less basis in observation than the fast- versus slow-axis distinction, is one regarding off-symmetry axis velocity behavior. In the hexagonal case, maximum and minimum velocities only describe the symmetry axis and the plane perpendicular to it, and a unique definition of hexagonal symmetry requires a parameter that describes the phase velocity behavior between the symmetry axis and symmetry plane. In the Backus representation (Appendix A), the azimuthal velocity variation as a function of incidence angle θ relative to the symmetry axis is described by $\cos(2\theta)$ term with amplitude b and a $\cos(4\theta)$ term with amplitude c. When $c = 0$, the phase velocity has an ellipsoidal shape, with increasing c corresponding to increasing deviation from the elliptical anisotropy case. Figure 2c shows c for all samples in the compilation. Deviation from ellipticity increases with increasing elliptical anisotropy, b (which itself scales to total anisotropy, Figure 1a). To illustrate the effect of the 4θ term on the phase velocity surface, we show the latter in Figure 2d. The effect of the off-axis velocity is more easily described using a different parameter as follows.

Another commonly used representation of off-axis behavior is the shape factor η, defined as $\eta = F/(A - 2L)$ [*Anderson*, 1961; *Takeuchi and Saito*, 1972] in terms of Love coefficients (Appendix A). The shape factor has no straightforward physical meaning and can introduce unphysical effects when varied independently of strength of anisotropy [*Porter et al.*, 2011]. It is unknown what values of η are representative for crustal anisotropy. Occasional references to a range of values for the shape factor of 0.4–0.9 are based on one ultrasound study of five foliated samples [*Godfrey et al.*, 2000].

Kawakatsu et al. [2015] and *Kawakatsu* [2016] introduced a different parameter they named η_κ, defined as $\eta_\kappa = (F + L)/[(A - L)^{1/2}(C - L)^{1/2}]$. This new parameter has a straightforward geometrical interpretation in that the velocity surface is ellipsoidal if $\eta_\kappa = 1$. We refer to this parameter as the ellipticity parameter. *Kawakatsu* [2016, Figure 3 therein] shows how the phase velocity surface varies when the ellipticity parameter deviates from 1; $\eta_\kappa < 1$ implies that the off-axis qP velocity surface is squashed inward from an elliptical shape (red curves in Figure 2d), while $\eta_\kappa > 1$ implies that the off-axis qP velocity surface is inflated outward (toward higher velocities) from an elliptical shape (blue curves in Figure 2d). In some cases, the minimum velocity occurs at an oblique angle from the symmetry axis (Figure 2d; red curves in the slow-axis symmetry group). The phase velocity changes in the opposite sense for shear waves [*Kawakatsu et al.*, 2015]. In the absence of information on appropriate values for η or η_κ for crustal anisotropy, an assumption made in many receiver function anisotropy studies [*Levin and Park*, 1998; *Levin et al.*, 2002a, 2002b; *Ozacar and Zandt*, 2004; *Sherrington et al.*, 2004; *Levin et al.*, 2008; *Ozacar and Zandt*, 2009; *Porter et al.*, 2011; *Bianchi et al.*, 2015; *Liu et al.*, 2015; *Licciardi and Agostinetti*, 2016; *Park and Levin*, 2016] is that the off-axis velocities follow an elliptical pattern, i.e., that $\eta_\kappa = 1$.

We calculate *Kawakatsu* [2016] ellipticity parameter η_κ using the best fit hexagonal tensor for all samples in the compilation. The results (Figure 3a) show that anisotropy deviates systematically from the elliptical case as a function of anisotropy, with a large majority of samples showing a decrease in η_κ with increasing anisotropy (i.e., off-axis Vp is smaller than in the elliptical case). This trend is particularly pronounced for mica-rich samples (red/purple points in Figure 3a). Amphibolites (green) follow a trend that has the same sense but is less pronounced, while a few quartz-rich samples (blue) plot with positive η_κ indicating off-axis Vp larger than expected in the elliptical case. We provide empirical scaling relationships for each trend in section 4.1. These scaling relationships provide the crustal equivalent to scaling for the mantle as shown by *Becker et al.* [2006, Figure 8].

The ellipticity parameter η_κ is not only useful because of its geometrical interpretation but also because it is more stable than the shape factor η. Figures 3b and 3c show that the ellipticity parameter η_κ remains in a stable and narrow range from slightly above 0.6 to less than 1.2 for all samples, while the shape factor η
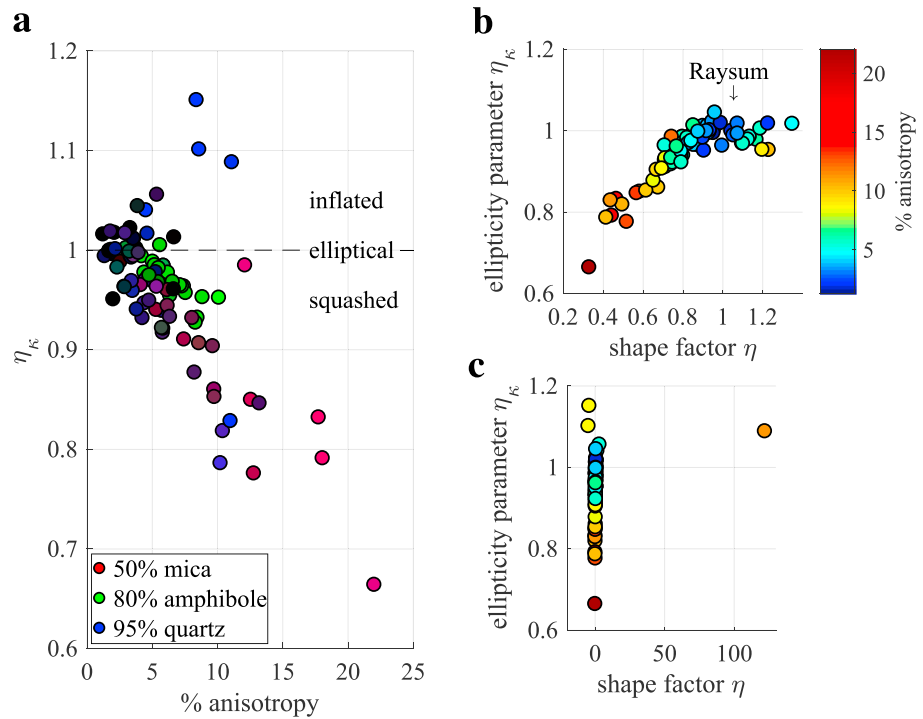
Figure 3. (a) Ellipticity parameter η_κ [*Kawakatsu*, 2016] as a function of strength of anisotropy. Each circle represents one sample from the compilation, with color fill coded by mineral composition on the same ternary red-blue-green scale as in Figure 5a; the minerals and their maxima are shown in the legend. Each color is scaled to the maximum percentage of the corresponding mineral in the compilation. Dark samples are from some ultrasound studies with no modal compositions reported. (b) Shape factor η for each sample as a function of ellipticity parameter η_κ, with color fill scaled by strength of anisotropy. Arrow shows the hardwired value of $\eta = 1.03$ in the popular Raysum code [*Frederiksen and Bostock*, 2000], which targeted mantle anisotropy. A common assumption, particularly in receiver function studies, is to set $\eta_\kappa = 1$ (elliptical case), but most crustal samples deviate toward smaller values for the shape factor with increasing anisotropy. (c) Full view of the same plot and same color scale that includes the three quartz-rich outliers in this plot with "inflated" off-axis Vp (Figure 3a), with values for the shape factor near -4 and 120, respectively.

shows outliers for the same sample set. Apart from the outliers (Figure 3b; seen to be quartz-rich samples in Figure 3a), shape factor and ellipticity parameter scale to each other and both decrease with increasing anisotropy (Figure 3b). Some receiver function studies may use the hardwired shape factor value of $\eta = 1.03$ from the original publication of *Frederiksen and Bostock* [2000], which was chosen for mantle studies [*Farra and Vinnik*, 2000] and is not an appropriate choice for most crustal rocks.

3.4. Tensor Symmetry Groups

The tensors can be visualized by calculating velocities for every possible propagation direction using the Christoffel equation and contouring them on a stereographic projection or stereonet plot. A few symmetry groups become evident when the tensors are visualized rather than simply using the proportion of each symmetry component from the decomposition. Figure 4 shows stereonets of Vp for representative tensors from seven symmetry groups and their low-anisotropy equivalents. First, the tensors can be grouped based on whether their best fit hexagonal component tensor has a slow symmetry axis or a fast symmetry axis. Within those groups, there are tensors that appear dominantly hexagonal, have a noticeable orthorhombic component, or have lower order symmetry. The stereonets highlight the orthorhombic component even when its contribution to the total tensor may not be very large compared to the hexagonal component. This is particularly true for Vp, whereas the Vs symmetry tends to appear more complex because of the tendency of the fast shear wave to switch polarization orientations in different propagation directions. For both fast and slow-axis hexagonal symmetry groups, the tensors are nearly equally split between dominantly hexagonal and dominantly orthorhombic symmetry in Vp. The slow-axis group has more tensors in total and also contains more tensors that are a combination of hexagonal and orthorhombic symmetry. There is a gradient
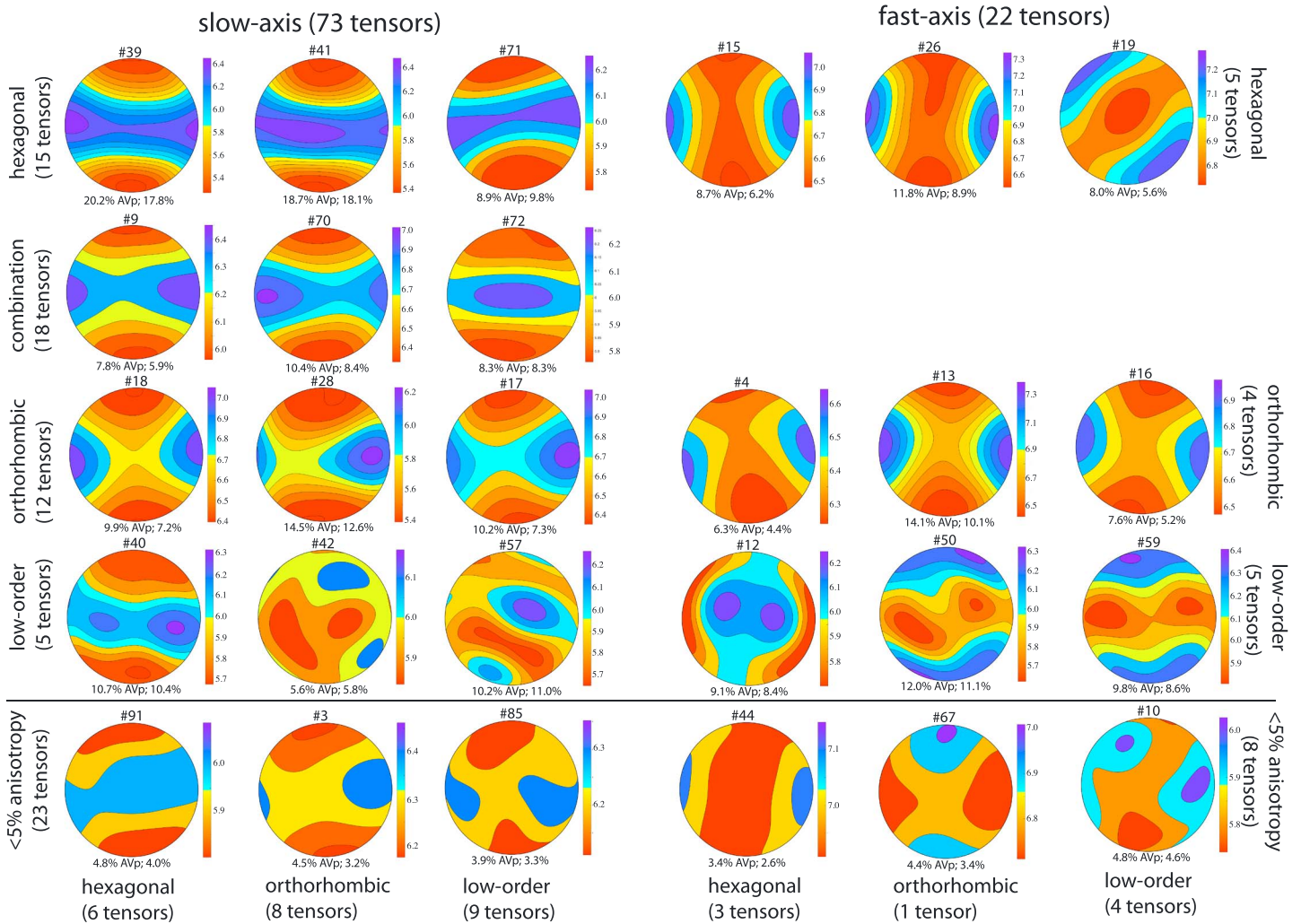
Figure 4. Lower hemisphere Vp stereonets for representative tensors illustrating the tensor symmetry groups found in the compilation. Contours are 0.1 km/s. Color scales vary for each tensor; we focus on symmetry appearance rather than absolute velocities in this figure. Sample numbers are shown above each stereonet, tensor anisotropy in percent, and % AVp below. Matrix is arranged with slow-axis tensors on the left, fast on the right, with rows from top to bottom sorted by dominant hexagonal symmetry, hexagonal with some orthorhombic symmetry, significant orthorhombic symmetry, lower order symmetries, and weak anisotropy.

between dominantly hexagonal and dominantly orthorhombic symmetry. There are also some tensors in both the slow- and fast-axis groups that appear to have more low-order symmetry. The tensors with lower magnitude of anisotropy fall into similar symmetry groups, but there are a few more low-anisotropy tensors in the low-order symmetry group.

### 3.5. Anisotropic Symmetry Components as a Function of Rock Type

Grouping the tensors into symmetry groups reveals some recognizable trends in symmetry with respect to rock type. The first obvious trend is that there are no schists in the fast-axis symmetry category. Schists are defined by having a foliation fabric of visibly aligned micas and therefore must contain significant amounts of mica. Micas are sheet silicate minerals with very high single-crystal anisotropy (>50% in Vp) and dominantly hexagonal symmetry with a slow symmetry axis. It is thus not surprising that rocks identified as schists will have slow-axis symmetry in their hexagonal component tensor. A trend in the fast-axis symmetry category is that most of the rocks are amphibolites (27%), quartzofeldspathic gneisses (27%), or plutonic rocks without gneissic layering (14%). All of the rocks in the fast-axis category are rich (~ > 45% by volume) in one of three minerals: quartz, amphibole, or feldspar (plagioclase + K-feldspar). Five samples have >50% quartz, seven have >50% amphibole (hornblende), and seven have >47% feldspar. None of the samples
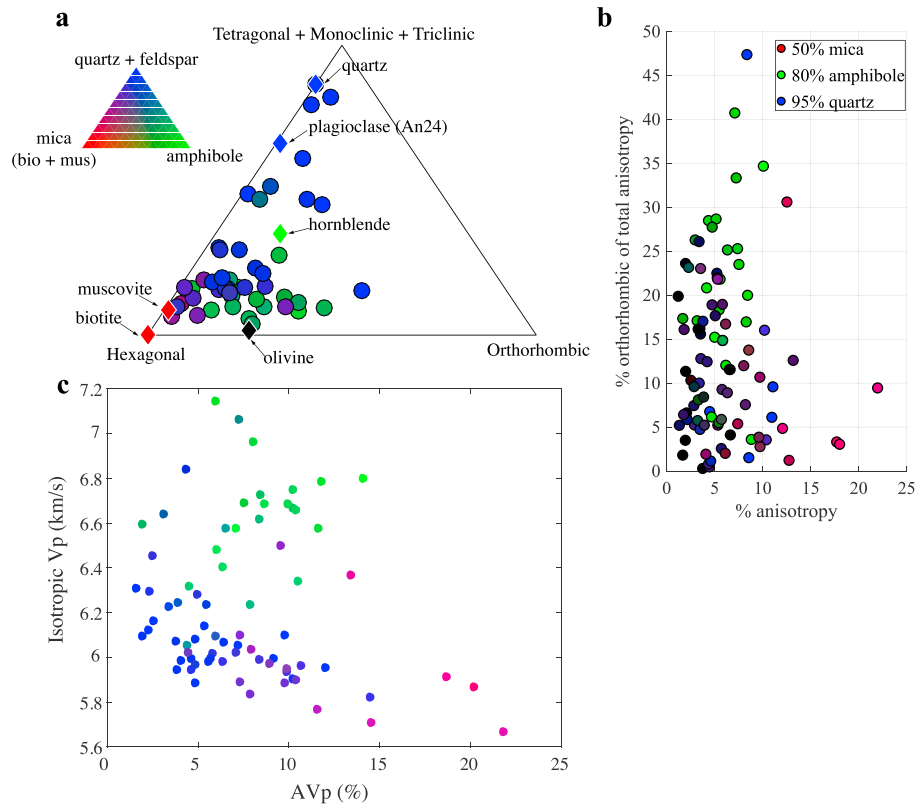
Figure 5. (a) Ternary diagram showing the fraction of hexagonal to orthorhombic to lower symmetry components (axes) as a function of composition (inset; continuous ternary red-blue-green color scheme separating mica, quartz + feldspar, and amphibole) for all samples in the compilation with anisotropy of 5% or higher, and modal compositions of those minerals totaling at least 80%. The positions of single-crystal hornblende (an amphibole), micas (muscovite and biotite), plagioclase (a feldspar), and quartz are shown as diamonds for comparison. The samples with lower anisotropy show the same trends, but we omit them to minimize crowding of the diagram. Single-crystal tensors are from *Lakshtanov et al.* [2007] for quartz at 20°C, *Aleksandrov and Ryzhova* [1961a, 1961b] for hornblende and biotite, *Vaughan and Guggenheim* [1986] for muscovite, and *Ryzhova* [1964] for plagioclase (An24). (b) Scatterplot showing the orthorhombic component as portion of the total anisotropy for all samples, displayed as a function of the strength of anisotropy of the sample. Color coding is the same as in Figure 5a, except with colors scaled to the maximum modal occurrences of the respective minerals (shown in inset). Dark samples are from some ultrasound studies with no modal compositions reported. (c) Isotropic, or average Vp, combined with anisotropy can be used to distinguish samples that are rich in quartz-feldspar, mica, or amphibole. The color scheme is the same as in Figure 5b, where red-green-blue values are assigned as red = mica, green = amphibole, and blue = quartz + feldspar. Actual values are normalized by the maximum value for that mineral. Tensors for which modal proportions for quartz, feldspar, mica, and amphibole were less than 80% total (*N* = 17) are not included here and would include the calc-silicates and many of the ultrasonic studies.

in the fast-axis category contain more than 10% mica. In general, fast-axis symmetry occurs only when a single mineral, or a mineral group (i.e., feldspar), dominates the composition of the rock and when the mica content is less than ~10%.

Most (77%) of the tensors in the compilation fall into the slow-axis symmetry category. This category contains mostly quartzofeldspathic gneisses (40%), schists (20%), and plutonic rocks (16%), but all rock types are found in the slow-axis symmetry category. The biggest difference between the fast- and slow-axis symmetry categories are in the proportion of amphibolites and gneisses. There are proportionately more amphibolites in the fast-axis category, with 27% compared to only 9% in the slow-axis category. Within the slow-axis category, the dominantly hexagonal group contains only 1 amphibolite out of 14 tensors and consists of 50% gneisses. The dominantly orthorhombic group contains 2 amphibolites out of 12 tensors but also contains 2 other amphibole-rich rocks. The largest group in the slow-axis symmetry category is a combination of hexagonal and orthorhombic symmetry. This group contains 5 amphibolites out of 19 tensors.
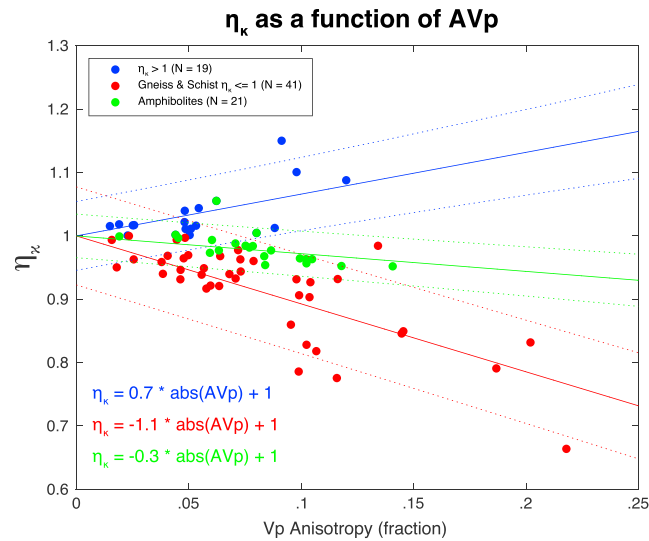
Figure 6. Three scaling relationships for η_κ as a function of AVp (fractional rather than %). Line fits are shown with 90% confidence intervals. Red samples are gneisses and schists with negative η_κ; green samples are amphibolite population; and blue samples are all nonamphibolite samples with $\eta_\kappa > 1$. The choice of these three populations was made to best represent different trends with composition seen in Figure 3a.

3.6. Strength of Orthorhombic and Lower Symmetry Components and Relationship to Composition

The significant symmetry components in all of the tensors are isotropic, hexagonal, orthorhombic, and triclinic. Tetragonal components are much smaller than 1% for all samples, and monoclinic components are smaller than 1% for all but three samples. If we only consider the anisotropic components, we have essentially a three-symmetry component system that lends itself well to visualization on a ternary diagram. According to the three anisotropic symmetry components, hexagonal, orthorhombic, and remaining symmetry (tetragonal + monoclinic + triclinic), we notice that all of the samples plot roughly on the hexagonal half of the diagram (Figure 5a), suggesting that hexagonal symmetry is indeed the most dominant contribution to anisotropy.

However, when color coded according to mineralogy (red = mica, green = amphibole, blue = quartz + feldspar), the symmetry contributions of particular minerals become apparent. For example, when minerals such as quartz and feldspar are dominant in the sample (blue dots), the symmetry is dominated by the low-order symmetry components. Likewise, when a rock contains large amounts of mica (red-purple dots), the hexagonal symmetry component is dominant. For reference, the single-crystal symmetry components of a few common minerals, quartz, feldspar, biotite, muscovite, hornblende, and olivine, are included on the ternary diagram. The contribution of a particular mineral within a rock depends on its single-crystal symmetry and its CPO. For example, hornblende does not have a particularly high component of orthorhombic symmetry in its single-crystal elastic tensor, i.e., it is not located very near the orthorhombic corner of the ternary diagram, but rocks with large amounts of hornblende tend to have higher orthorhombic symmetry components due to the common hornblende CPO. This can be seen in Figure 5a by a general preference for the greener dots to be closer to the orthorhombic corner of the ternary diagram than any of the other colored symbols.

A scatterplot of the contribution of the orthorhombic component to total anisotropy (Figure 5b) shows similar trends. This figure also shows trends with the total strength of anisotropy, where amphibolites (green) have a noticeably stronger orthorhombic contribution than quartz- (blue) or mica-rich (red/purple) samples. Only one sample each with significant quartz or mica show a large orthorhombic component. Samples rich in mica (red/purple) show higher total anisotropy.

Finally, when average or isotropic Vp is plotted along with AVp (Figure 5c), there is quite good separation between the amphibole-rich, quartz-feldspar-rich, and mica-rich samples. The mica-rich (pink-red) samples are spread out toward lower Vp and higher anisotropy, while the quartz-feldspar-rich samples are concentrated at lower average Vp and anisotropy. Some of the more feldspar-rich samples have higher average Vp and low anisotropy. The amphibole-rich samples have higher average Vp, and their higher anisotropy separates them from the feldspar-rich samples.

4. Discussion

4.1. Simple Empirical Scaling Relationships for η_κ With Anisotropy

While seismic methods for determining elastic tensors from seismic data often assume elliptical hexagonal symmetry (in the absence of information constraining off-axis velocities), results from the symmetry decomposition of the elastic tensors in our compilation suggest that elastic tensors from crustal rocks are not

likely to be elliptical in their hexagonal symmetry component. The assumption of elliptical symmetry makes the full unique elastic tensor a function of density, orientation of the symmetry axis (trend and plunge), and four independent elastic parameters that can be expressed in terms of average Vp, average Vs, percent Vp anisotropy, and percent Vs anisotropy. Nonelliptical symmetry requires an additional fifth elastic free parameter to describe velocities between the symmetry axis and symmetry plane. Our tensor compilation suggests an approximately linear scaling between the ellipticity parameter η_κ and anisotropy. A simple scaling relationship allows inclusion of nonelliptical behavior without increasing the free parameters in the inversion, which means inversions will produce tensors that are more consistent with measured rock tensors.

Our tensor compilation provides three useful scaling relationships for η_κ as a function of AVp for a few different groups (Figure 6). The scaling relationships were determined using a least squares linear fit to the data with a fixed y intercept of 1, because η_κ is equal to 1 for isotropic tensors. The first scaling relationship is for the 19 inflated hexagonal tensors, those with η_κ greater than 1. These are mostly fast-axis tensors, and they show a positive scaling between η_κ and fractional AVp, with a slope of 0.7. The next is for the gneiss and schist rock types, which include most of the compilation, 41 tensors. These show a negative scaling with η_κ, with a slope of −1.1. Interestingly, the 21 amphibolite tensors show smaller deviations from the elliptical case, with a slope of −0.3. These scaling relationships provide a simple alternative to the elliptical approximation, with the most commonly applicable case expected to be that for gneisses and schists, $\eta_\kappa = 1–1.1$ AVp (where AVp is fractional AVp). We provide expressions for η_κ in terms of other sets of hexagonal coefficients in Appendix A.

4.2. Effects on Seismic Signatures and Interpretation

We proceed to describe the seismic expression of the tensor characteristics in our compilation, in particular in receiver functions. *P* receiver functions register anisotropy in two ways. The first is splitting of the *P*-to-*S* converted phase [*McNamara and Owens*, 1993; *Peng and Humphreys*, 1997], which accumulates in anisotropic layers above the converting contrast. Anisotropy of significant magnitude and thickness is required to accumulate a measurable signal, and while the technique has experienced a recent resurgence in popularity for estimating bulk crustal anisotropy from splitting of the Moho *Ps* phase [*Nagaya et al.*, 2008, 2011; *Liu and Niu*, 2012; *Sun et al.*, 2012; *Ruempker et al.*, 2014; *Shen et al.*, 2015; *Sun et al.*, 2015; *Kong et al.*, 2016; *Niu et al.*, 2016; *Wang et al.*, 2016], it will not detect shear zones of a few kilometers thickness and a few percent contrast in anisotropy, and splitting may be conflated with conversions from thinner anisotropic layers [*Liu and Park*, 2017]. A second receiver function method that is capable of resolving such structures robustly is based on analyzing azimuthal variations in the amplitude and polarity of converted phases. These have significant amplitude even for thin layers and anisotropy contrasts of a few to 10%, which we expect to be best represented by the anisotropy in our compilation. The conversions are mostly sensitive to Vp anisotropy [*Levin and Park*, 1998; *Park and Levin*, 2016], which we focus on in this contribution.

4.2.1. Receiver Function Appearance for Different Symmetry Types

We first present synthetic waveforms for out-of-plane *P*-to-*S* converted phases for some of the example tensors shown in Figure 4. We use the ray-based Raysum code [*Frederiksen and Bostock*, 2000] for the forward modeling, with a modification where the entire elastic tensor is read in as input for an anisotropic layer, rather than being constructed from isotropic velocities, percent Vp and Vs anisotropy, and hardwired shape factor as in the original. The complete sample tensors are first rotated into their best fit hexagonal coordinate systems for consistency, since the tensors are reported in varying orientations in the original publications. Each tensor is then inserted into a horizontal layer within the crust, surrounded by homogeneous isotropic crust above and below, for calculation of the waveforms. The anisotropic layer thickness is set to 15 km, not because we expect this thickness of coherent anisotropy in the crust to be realistic but to clearly separate the topside and bottomside converted phases in the figures. The signals analyzed in the receiver function azimuthal conversion method are the conversions from the interface marking a contrast in anisotropy, so that the layer thickness is required to be sufficient to separate the topside and bottomside conversions in time. In reality, layers of ~2 km thickness may be resolved, depending on frequency content and Vp/Vs ratios within the layer [*Schulte-Pelkum and Mahan*, 2014a, 2014b]. Thinner layers result in the same conversion amplitudes. The only difference is the time separation between the topside and bottomside conversions.

Figure 7a shows radial component waveforms for sample 28 (Figure 4), a slow-axis dominantly hexagonal tensor with 13% total tensor anisotropy and 14.5% AVp anisotropy. Here the tensor is oriented so that the
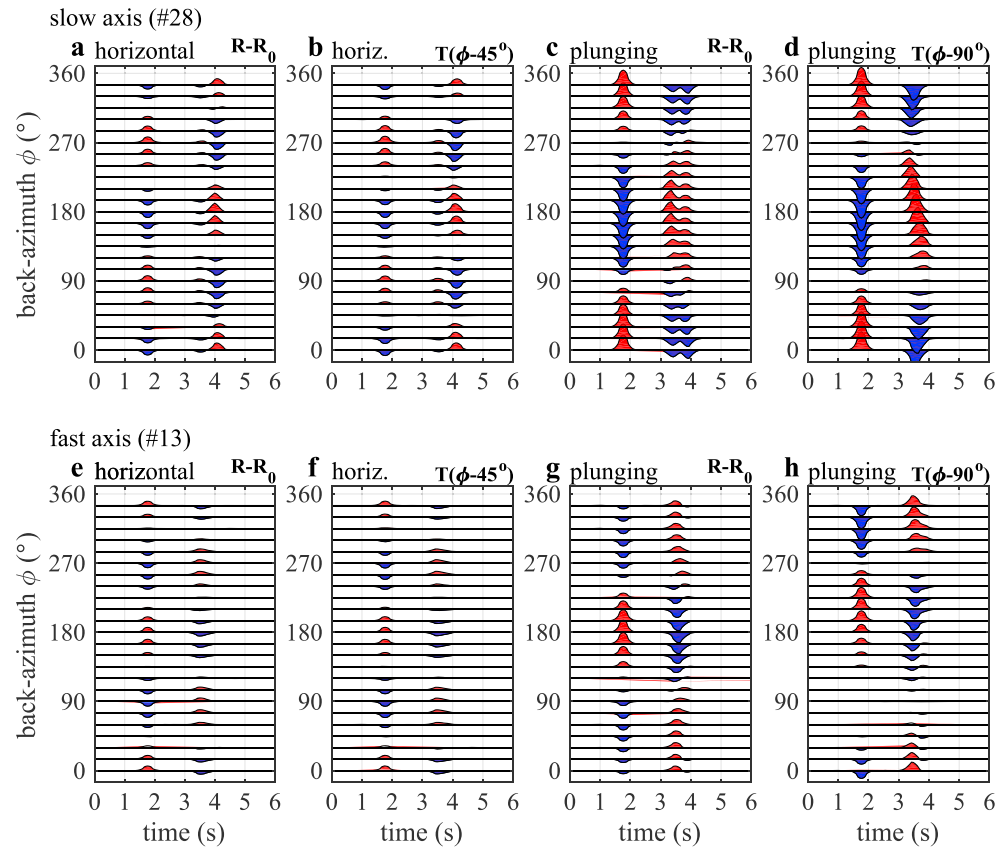
Figure 7. (a) Synthetic radial component seismograms for model with 15 km thick anisotropic layer sandwiched from 15 to 30 km depth within isotropic crust. The anisotropic layer consists of sample 28, which has slow-axis best fit hexagonal anisotropy with an orthorhombic component and 13% total tensor anisotropy. Incident slowness is set to 0.06 s/km. Traces calculated for incidence from every 15° back azimuth, with subsequent azimuthal average trace (R_0) subtracted from each trace to isolate the out-of-plane signal that varies with back azimuth. Arrival at ~1.8 s is the P-to-S conversion from the top of the anisotropic layer; arrival at ~4.1 s is from the bottom of the anisotropic layer. The latter shows a slight split of the converted shear wave accumulated during travel through the anisotropic layer. Note the four-lobed (degree-2, A2) pattern. (b) Same as Figure 7a but transverse component, with a shift in back azimuth (i.e., along y axis) of 45° to show the match to the out-of-plane radial component in Figure 7a. (c) Out-of-plane signal in radial component as in Figure 7a, but here for the same tensor with a 35° symmetry axis plunge from horizontal (i.e., 55° dipping foliation plane). (d) As in Figure 7b but also for plunging axis tensor. Note the two-lobed (degree-1, A1) pattern in Figures 7c and 7d, as well as larger conversion amplitudes for the same tensor compared to the horizontal axis case in Figures 7a and 7b (the same amplitude scaling is used in all panels). (e–h) As in Figures 7a–7d but for a fast-axis symmetry tensor (sample 13, see Figure 4) with 8% tensor anisotropy.

axis of the best fit hexagonal symmetry is horizontal. The azimuthally averaged radial component arrival amplitude is only a function of the contrast between the average velocity in the anisotropic layer and the surrounding layers and is removed by subtracting the azimuthal stack trace R_0 from the individual traces for each back azimuth; note that this removes the direct P arrival at zero time entirely. The remaining signal shown in Figure 7a is the out-of-plane signal on the radial component [*Schulte-Pelkum and Mahan*, 2014b]. The earlier arrival (~1.8 s delay time after direct P arrival) is the conversion from the top of the anisotropic layer (delay time always scales with depth for receiver functions). It shows a four-lobed pattern with back azimuth that is characteristic for azimuthal (i.e., horizontal symmetry axis) anisotropy. The later arrival (~4.1 s) is the conversion from the bottom of the anisotropic layer. It has a polarity pattern opposite that of the topside conversion. In addition, this arrival shows splitting accumulated by the converted shear wave during propagation through the anisotropic layer. The observation target in our method is the azimuthal amplitude variation of the conversions and not the splitting signal. Even for the synthetic cases here with a large anisotropic layer thickness of 15 km with a relatively strong coherent anisotropy of 13%, the splitting of the bottomside conversion is 0.5 s. In realistic cases with thinner layers of crustal anisotropy

(e.g., shear zones), the splitting will be significantly less, and observational evidence places most around a maximum of ~0.3 s, although crustal splitting values up to ~1 s have been proposed for the thick crust of Tibet [*Sun et al.*, 2015; *Niu et al.*, 2016].

Transverse component receiver functions in general only show arrivals in cases with dipping interfaces or contrasts in anisotropy. Figure 7b shows transverse component waveforms for the same model and same tensor as in Figure 7a, also for horizontal symmetry axis orientation. The traces were shifted by 45° in back azimuth to emphasize the similarity of the polarity and amplitude pattern to that of the out-of-plane signal on the radial component [*Schulte-Pelkum and Mahan*, 2014b]. The azimuth-shifted transverse and the average-corrected radial components are nearly identical. At amplitudes of ~0.1 *H/Z*, the arrivals roughly are about a third of a standard Moho arrival amplitude and should be visible at quiet stations in real data.

When inserting the same tensor after rotating it to generate a symmetry axis that is tilted within the horizontal anisotropic layer, out-of-plane conversion amplitudes are significantly larger (Figure 7c), an observation made previously both via forward modeling [*Levin and Park*, 1998; *Schulte-Pelkum and Mahan*, 2014b] and theory [*Park and Levin*, 2016]. The out-of-plane signal amplitude on both the radial (Figure 7c) and transverse (Figure 7d) components is now comparable to that of a strong radial component Moho signal in standard receiver function analysis. The dominant azimuthal harmonic is now a two-lobed or degree-1 pattern, termed A1 here, and the transverse component was shifted in back azimuth by 90° (Figure 7d) to show the correspondence in the polarity pattern.

Figures 7e–7h show similar synthetic waveforms for a tensor with fast-axis symmetry, rather than slow axis as in the previous figure. The tensor anisotropy strength is 8% (9% AVp), and the dominant symmetries are hexagonal with a significant orthorhombic component (Figure 4). The horizontal axis orientation results in arrivals with purely A2 (degree-2, four-lobed) azimuthal periodicity (Figures 7e and 7f), while the plunging axis case shows a mix of A1 and A2 components (Figures 7g and 7h), unlike the previous tensor (Figures 7c and 7d). The polarities of the arrivals are also reversed compared to the slow-axis case, as expected.

The maximum amplitudes of the topside conversion over all incidence back azimuths are displayed as a function of symmetry axis plunge for seven example tensors in Figure 8, with the calculations performed with the same code. The amplitude is the highest over all back azimuths on the transverse component. Also shown are the A1 and A2 amplitudes of the harmonic azimuthal decomposition [*Schulte-Pelkum and Mahan*, 2014b] and the degree to which the first two azimuthal harmonics reproduce the maximum observed out-of-plane arrival amplitude. Figure 8b shows results for sample 28 also used in Figures 7a–7d, and Figure 8e is the same tensor as for Figures 7e–7h. Figure 8 shows representative calculations for fast- and slow-axis hexagonal (Figures 8a and 8d), orthorhombic (Figures 8b, 8c, and 8e), and low-order symmetry (Figures 8g and 8h) cases. In most cases, the first two azimuthal harmonics reproduce the total signal amplitude very closely; slight exceptions are seen for one fast-axis hexagonal case (Figure 8d) and a low-order case (Figure 8h), with another low-order symmetry sample showing larger deviations (Figure 8g). All higher-order symmetry cases show dominant A2 periodicity in conversions for the horizontal symmetry axis/azimuthal anisotropy case (plunge = 0°) as well as dominant A1 periodicity for the plunging axis case, with minimal amplitudes for the case where the best fit symmetry axis is vertical (plunge = 90°). Figures 8f and 8i show the breakdown of the compilation in terms of symmetry classes and strength of anisotropy. Slow-axis best fit hexagonal symmetry dominates, and a significant number of samples show a noticeable orthorhombic influence in the stereoplots (Figures 8f and 4). However, the azimuthal amplitude behavior is similar between dominant hexagonal tensors and those with a significant orthorhombic component (Figures 8a–8e). The ratios of the number of samples with stronger (>5%) and weaker (<5%) anisotropy are comparable between the fast and slow best fit symmetry cases (Figure 8i).

### 4.2.2. Effect of Off-Axis Symmetry (Deviation From Ellipticity) on Receiver Functions

We determined in section 3.5 that the elliptical assumption for the best fit hexagonal tensor component does not hold for our tensor compilation and that the deviation from ellipticity scales with the strength of anisotropy. We investigate the effect of this behavior on observed receiver function conversions in this section. Studies that model or invert receiver function conversion amplitudes to determine strength of anisotropy commonly assume elliptical anisotropy [*Levin and Park*, 1998; *Levin et al.*, 2002a, 2002b; *Ozacar and Zandt*, 2004; *Sherrington et al.*, 2004; *Levin et al.*, 2008; *Ozacar and Zandt*, 2009; *Porter et al.*, 2011; *Bianchi et al.*, 2015; *Liu et al.*, 2015; *Park and Levin*, 2016; *Licciardi and Agostinetti*, 2016], and we are interested to what extent the latter assumption will bias the inferred strength of anisotropy.
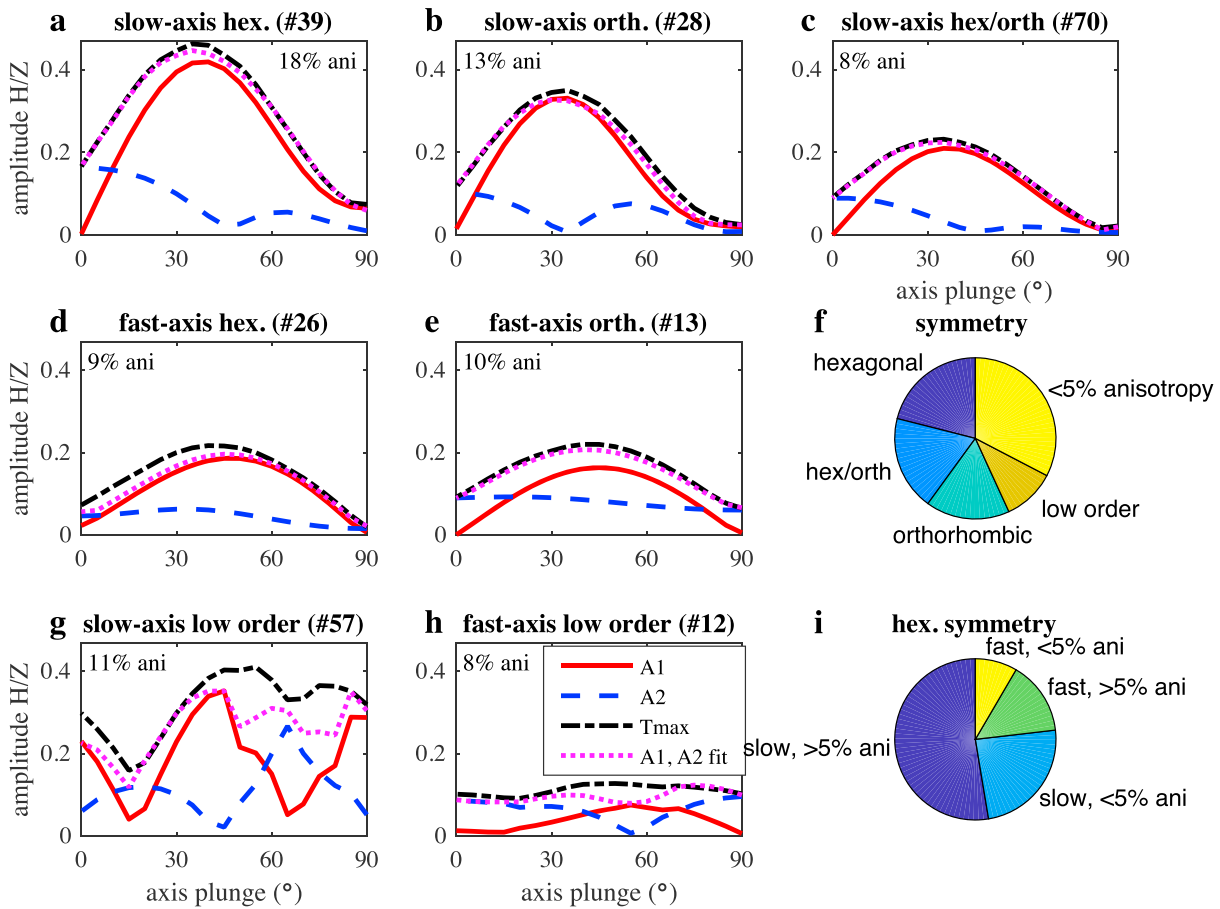
Figure 8. (a) Receiver function amplitudes (black dash-dotted, maximum transverse component Tmax; red solid, degree-1 azimuthal harmonic fit amplitude A1; blue dashed, degree-2 azimuthal harmonic fit amplitude A2; pink dotted, reproduction of Tmax by A1 and A2 combined, including azimuthal phase relationship; see Figure 8h for the legend). Amplitudes are shown as functions of best fit hexagonal symmetry axis plunge in degrees from horizontal (0 = azimuthal anisotropy approximation with horizontal symmetry axis, 90 = radial anisotropy approximation with vertical symmetry axis), for example, sample tensors shown in Figure 4. An intermediate ray parameter of 0.06 s/km is used for calculating all synthetic receiver functions. Sample 39 (sample number shown on top) is an example for a tensor well approximated by slow-axis hexagonal symmetry (Figure 4; all tensors used for this figure are displayed in Figure 4). Total tensor anisotropy shown as inset (18%). (b) Same as Figure 8a but for a slow-axis orthorhombic sample. (c) Same as Figure 8a but for a sample showing a mix of hexagonal and some orthorhombic symmetry. (d) Same as Figure 8a but fast-axis hexagonal symmetry. (e) Same as Figure 8a but fast-axis orthorhombic symmetry. (f) Pie chart of symmetry types found in compilation (hexagonal with total tensor anisotropy >5%, hexagonal with weak orthorhombic component and total tensor anisotropy >5%, strong orthorhombic component and total tensor anisotropy >5%, low-order symmetry, and any symmetry with total tensor anisotropy <5%). (g) Same as Figure 8a but dominant low-order symmetry with nominal slow hexagonal axis. (h) Same as Figure 8g but nominal fast hexagonal axis. (i) Pie chart of slow- (73 samples) and fast-axis (22 samples) best fit hexagonal symmetry in the compilation, each broken down into weak (<5%) and strong (>5%) total tensor anisotropy groups.

Figure 9 shows the maximum observed out-of-plane receiver function amplitude (Tmax) for each sample in the compilation. As in Figure 8, we use the maximum amplitude over all back azimuths calculated for the top-side conversion on the transverse component, and we again use a representative incident slowness of 0.06 s/km. The maximum amplitude is calculated for each sample for three orientations of the tensor: one for a best fit hexagonal symmetry axis plunge of 0° (closest to azimuthal anisotropy; red symbols in Figure 9); one for 90° plunge (closest to radial anisotropy; green symbols in Figure 9); and one for a plunge of 35° (symmetry plane dip of 55°, blue symbols in Figure 9), the plunge angle that maximizes the median maximum out-of-plane conversion amplitude over all samples for the assumed slowness.

The maximum amplitudes are shown twice, once as a function of tensor anisotropy and once as a function of AVp. They follow similar approximately linear trends, although scatter is reduced in the display using tensor anisotropy. As in Figure 8, conversions are largest for the plunging axis case, intermediate for the horizontal axis case, and small for the vertical axis case. Some outliers to this trend represent tensors with particularly low-order symmetry.
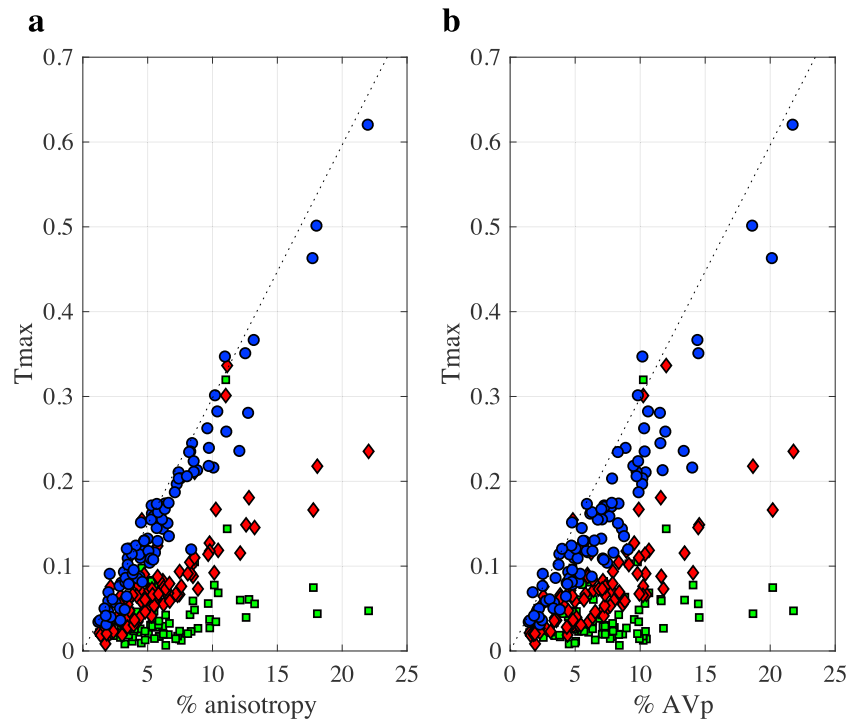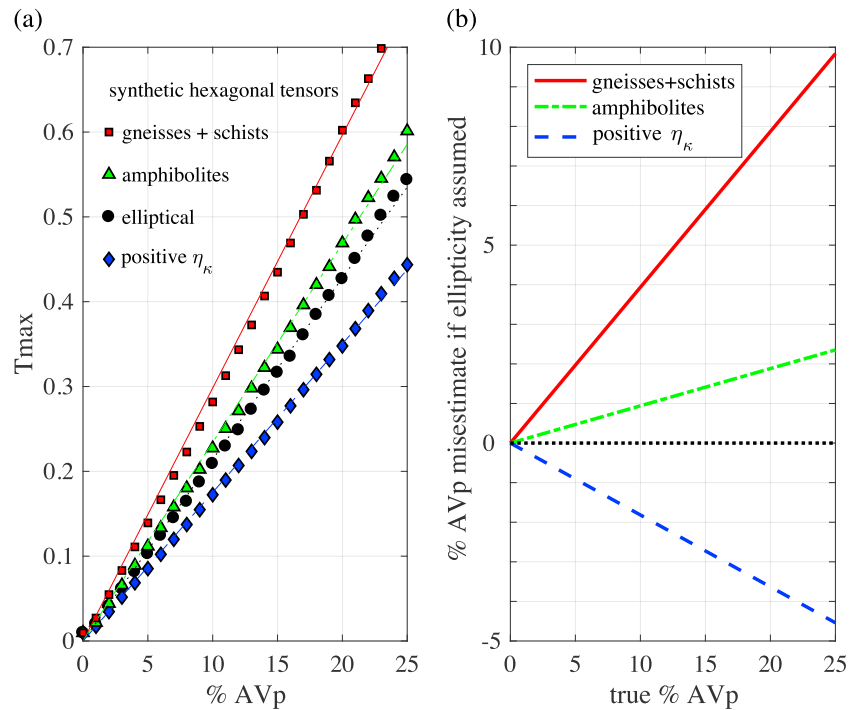
Figure 9. (a) Out-of-plane receiver function conversion *H/Z* amplitude (maximum amplitude over all back azimuths; abbreviated Tmax) for all sample tensors reoriented into best fit hexagonal systems; blue circles for 35° plunging symmetry axis (yielding maximum median amplitude for the chosen ray parameter of 0.06 s/km), red diamonds for 0° plunge (closest to azimuthal anisotropy orientation), and green squares for 90° plunge (closest to radial isotropy orientation), shown as a function of tensor norm anisotropy. (b) Same as in Figure 9a but shown as a function of AVp; note slightly larger scatter but similar linear trend. Dotted line in both panels is slope fit from synthetically constructed purely hexagonal symmetry tensors with gneiss/schist empirical ellipticity (red line in Figure 10a).

4.2.3. Quantitative Effect of Nonellipticity on Interpretation of Receiver Function Anisotropy

We proceed to estimate the bias introduced by the elliptical assumption by constructing synthetic hexagonal tensors that are either elliptical or follow our empirical scaling relationships for deviation from ellipticity from section 4.1 and predicting out-of-plane conversion amplitudes. Figure 10a shows predicted transverse component amplitudes (maximum over all back azimuths) for the three scaling relationships from section 4.1 and the elliptical case as a function of anisotropy strength, again using an incident ray parameter of 0.06 s/km, which is average for teleseismic *P* receiver functions. The amplitudes are nearly linear with strength of anisotropy (linear fits are shown). Figure 10b shows the amount by which the strength of anisotropy will be overestimated or underestimated by assuming ellipticity based on the linear trends in Figure 10a, shown as a function of input true AVp. As an example, if receiver function waveforms from an area with gneisses or schists with 10% true velocity anisotropy (AVp) were to be inverted assuming elliptical anisotropy, the observed anisotropy would be overestimated by an additional 4% for a total of 14% apparent elliptical anisotropy; for 15% true anisotropy, the apparent anisotropy would be 15% + 6% = 21% using the elliptical assumption. The bias is minimal for amphibolites (e.g., anisotropy will be overestimated by 1% for 10% true AVp). The bias is slightly larger in the opposite sense for the sample group with off-axis velocities exceeding ellipticity (e.g., close to 2% underestimate at 10% AVp). The bias is largest for the most common rock type in the compilation, gneisses and schists, where anisotropy would be overestimated by 40% of true anisotropy. The fit of the maximum amplitude as a function of AVp for gneisses and schists is overlaid on the observed maximum amplitudes for the tensor compilation in Figure 9 and provides a reasonable upper limit. The use of the elliptical approximation may explain some high values for crustal anisotropy resulting from receiver function inversions. For example, *Porter et al.* [2011] analyzed 38 stations for lower crustal anisotropy in Southern California, where there is presumed to be schist in the lower crust, using the elliptical assumption. They found the maximum anisotropy allowed by their inversion (20%) at 7 of the stations, with 29 stations having anisotropy of 10% or greater and 16 stations at 15% or greater. These values are high compared to the values in our

Figure 10. (a) Maximum synthetic out-of-plane receiver function amplitude calculated for synthetic hexagonal tensors constructed using ellipticity values predicted by the three empirical relationships in Figure 6, with linear line fits. Receiver function slowness of 0.06 s/km and slow hexagonal symmetry axis with plunge of 35° are used. Black circles and line show elliptical case for comparison. (b) Overestimation (positive on vertical axis) and underestimation (negative on vertical axis) of amount of anisotropy given an observed out-of-plane receiver function amplitude for different rock groups as a function of true anisotropy if elliptical anisotropy is assumed, using linear fits from Figure 10a. For instance, for gneisses and schists having $\eta_\kappa < 1$ with 10% true AVp, inverting receiver functions assuming elliptical symmetry would result in overestimating total AVp as 14% (an additional 4% over the 10% actual value), 15% would appear as 15% + 6% = 21%, and 20% would be overestimated as 28%. Inferred anisotropy will be 40% larger than actual anisotropy when assuming ellipticity for gneisses and schists.

compilation for schists (including Southern California schists) and would be lower using our nonelliptical scaling relationship.

4.2.4. Qualitative Effect of Off-Axis Scaling on Interpretation of Surface Wave Anisotropy

Surface wave results are most commonly inverted in terms of either radial anisotropy based on the Love-Rayleigh discrepancy [e.g., *Shapiro et al.*, 2004; *Moschetti et al.*, 2010; *Xie et al.*, 2013] or azimuthal anisotropy based on azimuthal variations of Rayleigh wave phase velocity [e.g., *Lin and Ritzwoller*, 2011] and *H/V* ratios [*Tanimoto and Rivera*, 2008; *Lin and Schmandt*, 2014]. Conceptually, there is no reason that the two types of anisotropy should exist independently or that anisotropy should be restricted to nonplunging axes, and *Xie et al.* [2015] extended the standard surface wave treatment to allow plunging hexagonal symmetry axes. They found that their inversion allowed two classes of solutions with equal fit to the data, one for elliptical hexagonal anisotropy and the other for nonelliptical anisotropy. Our compilation suggests that the latter is the more appropriate solution. Our observed values for the deviation from ellipticity match those in the nonelliptical solution set in *Xie et al.* [2015].

4.2.5. Accuracy of Hexagonal Symmetry Assumption in Receiver Function Analysis

In this section, we test how well the seismic signatures of complete elastic tensors in the compilation are represented by their hexagonal approximation. A long-standing question is whether orthorhombic symmetry (or lower symmetry components) cause bias when making the simplifying assumption of hexagonal anisotropy in seismic studies. We conduct tests with synthetic receiver function conversion amplitudes, again focusing on Vp anisotropy effects [*Park and Levin*, 2016].

Figures 11a–11f show transverse component synthetic waveforms for the same model as in Figures 7a–7d. The tensor used is that for sample 28, a slow-axis case with an orthorhombic component (Figure 4).
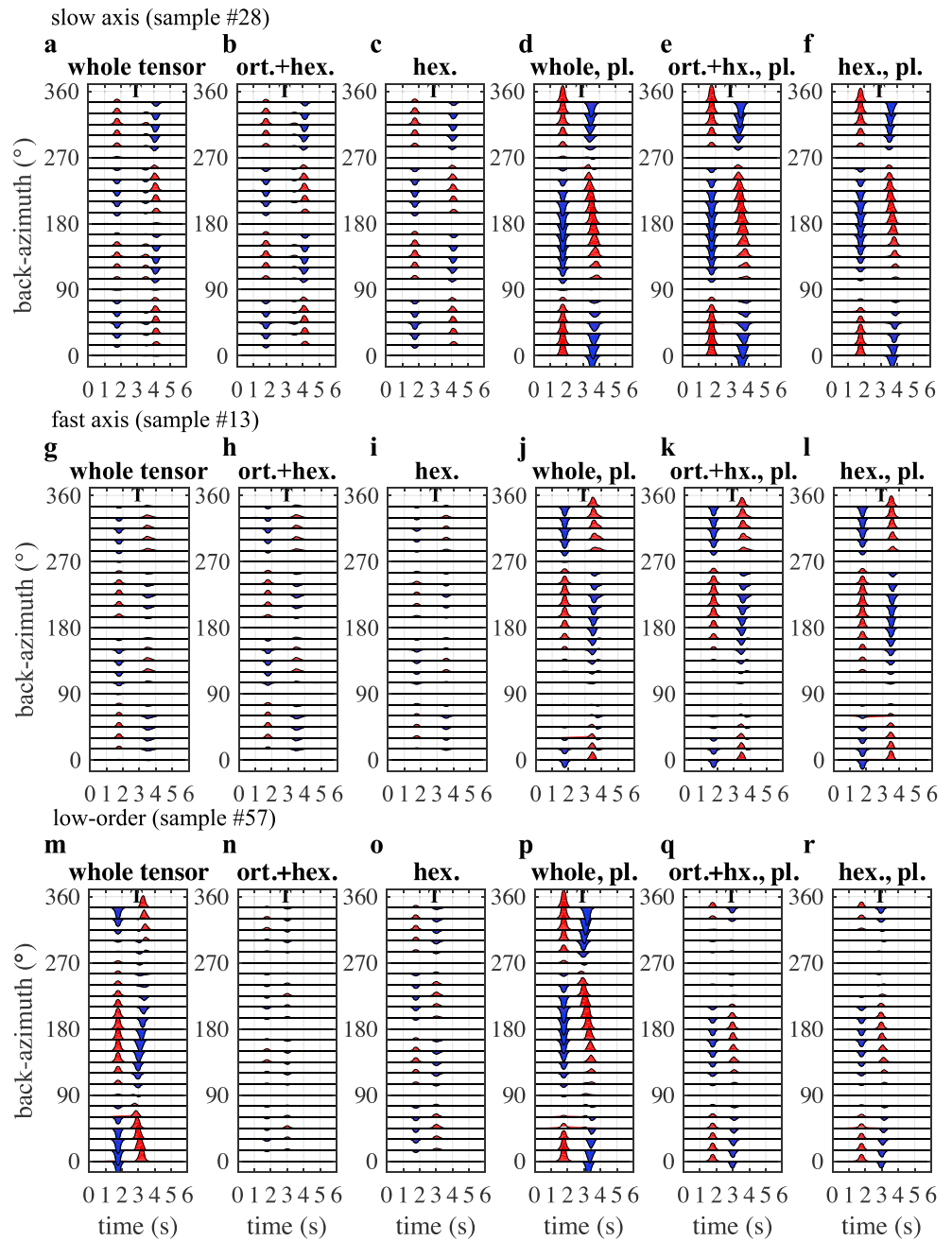
Figure 11. (top row) Synthetic transverse component waveforms for a model containing sample tensor 28 (slow axis hexagonal with orthorhombic pattern) sandwiched in a horizontal layer from 15 to 30 km depth in isotropic crust. Amplitude scale is the same in all panels in this figure. (a) "Whole tensor" uses the complete tensor with horizontal symmetry axis (plunge 0°); (b) "ort + hex" uses an approximate tensor represented by the hexagonal and orthorhombic components, omitting lower order components from the tensor decomposition, in the same horizontal symmetry axis orientation; (c) "hex." uses only the hexagonal component, also in horizontal symmetry axis orientation; (d) "whole, pl." is for the complete tensor with 35° symmetry axis plunge; (e) "orth + hex, pl" is for the hexagonal + orthorhombic approximation with plunging symmetry axis; (f) "hex. pl." for the hexagonal approximation with plunge. (g–l) As in Figures 11a–11f but for sample 13, a fast-axis hexagonal tensor with orthorhombic pattern. (m–r) As in Figures 11a–11f and Figures 11g–11l but for sample 57, a low-order symmetry tensor.

Synthetic waveforms are calculated as above, with slowness 0.06 s/km. We show waveforms calculated using the whole rock tensor, only the hexagonal component of the tensor, and the hexagonal + orthorhombic components, for the horizontal symmetry axis and plunging symmetry axis cases. The hexagonal and hexagonal + orthorhombic cases are a very close approximation of the waveforms calculated for the whole tensor, with no noticeable difference between the hexagonal versus hexagonal + orthorhombic cases and only very subtle differences from those to the whole tensor case. The same holds for another sample (sample13; Figure 4) that has fast-axis symmetry with an orthorhombic pattern (Figures 11g–11l). Similar observations hold for most tensors in our compilation. Only in the case of a strongly low-order symmetry tensor (sample 57; Figure 4) are the waveforms for the whole tensor significantly different from those calculated using the hexagonal or orthorhombic approximation (Figures 11m–11r). We conclude that the hexagonal approximation is close to accurate for receiver functions in most cases and that it may be difficult to separate orthorhombic from hexagonal symmetry using receiver function conversions.

4.2.6. Additional Factors Not Addressed by Our Compilation

A perennial question in studies of seismic anisotropy that attempt to relate seismic observations to rock fabric is that of scaling from microstructure to seismic wavelengths. In this study, we extrapolated from the microstructural (in the case of EBSD-, XTG-, and universal stage texture-derived tensors) or hand sample scale (in the case of ultrasound-derived tensors) to the seismic scale. In addition, all tensors from EBSD, XTG, and universal stage were calculated without taking the geometrical arrangement of the mineral modes into account; in reality, arrangement of the oriented grains in space within a sample may change its bulk elastic tensor [*Vel et al.*, 2016]. Both questions may now be addressed by a treatment of the arrangement of the grains in a microstructural scale [*Naus-Thijssen et al.*, 2011b, 2011a; *Vel et al.*, 2016] or spatial variations such as folding of layers with different compositions on the meter scale, 100 m scale, or kilometer scale [e.g., *Okaya et al.*, 2010]. However, our compilation provides a foundation on the microstructural and hand sample scale that future efforts for including geometrical effects can build upon.

This contribution does not discuss shear wave behavior, and the compiled samples do not exhaust the published literature, although we estimate that we have collected the majority of currently available published and possible author-contributed full elasticity tensors. Shear wave behavior and publication of the entire compilation will be the subject of a future publication.

5. Conclusions

We present an initial compilation of elastic tensors published for crustal rocks representing anisotropy below crack closure depth. Such data are necessary to provide ground truth for seismic observational and modeling studies, and we strongly encourage authors of future publications to include the complete elastic tensors (only 5 out of 12 studies used in the current compilation included the full elastic tensors). We observe that most samples are well approximated by hexagonal symmetry, that slow-axis hexagonal symmetry is more common in crustal samples, and that mica-rich rocks show slow rather than fast-axis symmetry, while amphibolites can fall in either category. Contrary to a popular assumption, samples deviate from elliptical hexagonal anisotropy with increasing strength of anisotropy, and we provide empirical scaling relationships to quantify this behavior, as well as estimates for the error incurred by assuming elliptical anisotropy. The elliptical assumption results in overestimation of anisotropy for common lower crustal rock types. Receiver function studies focused on crustal anisotropy should recognize the potential bias introduced by the elliptical assumption and consider introducing a scaling relationship into their inversions. We model the expression of the seismic anisotropy resulting from the full tensors in receiver function conversions, including conversion amplitudes and azimuthal harmonics. As for previously modeled purely hexagonal tensors, the full rock-based tensors show that horizontal symmetry axis orientations have dominantly degree-2 azimuthal receiver function amplitude behavior and plunging axis orientations have dominant degree-1. The scaling relationships derived from this compilation provide a stepping stone toward improving seismic inversions for crustal anisotropy. As the tensor compilation grows, more trends may be observed, and scaling relationships will be updated accordingly.

Appendix A: Ellipticity Parameter in Terms of Different Sets of Parameters for Hexagonal Symmetry Used in Seismic Studies

We presented empirical scaling relationships between deviation from ellipticity (Kawakatsu's ellipticity parameter η_κ) and strength of anisotropy in section 4.1, where η_κ was defined in terms of the Love coefficients. Here we provide expressions for η_κ in terms of two other commonly used sets of hexagonal elastic parameters (Backus and Thomsen parameters).

Backus parameters [*Backus*, 1965] are defined as follows:

$$\rho V_p^2 = a + b \cos 2\theta + c \cos 4\theta$$

$$\rho V_s^2 = d + e \cos 2\theta$$

where ρ is density; θ is the angle between the propagation direction and symmetry axis; and a is related to average Vp, b to azimuthal Vp anisotropy, c to ellipticity ($c = 0$ elliptical), d to average Vs, and e to azimuthal Vs anisotropy. The ellipticity parameter η_κ in terms of Backus parameters is

$$\eta_\kappa = \frac{a - 3c - d - e}{\sqrt{a+b+c-d-e} \; \sqrt{a-b+c-d-e}}.$$

Thomsen parameters [*Helbig and Thomsen*, 2005; *Thomsen*, 1986] are popular in surface wave studies [e.g., *Becker et al.*, 2006; *Xie et al.*, 2015]. They are defined in terms of Love coefficients as follows:

$V_{P0} = \sqrt{\frac{C}{\rho}}$ (P velocity along symmetry axis)

$V_{S0} = \sqrt{\frac{L}{\rho}}$ (S velocity along symmetry axis)

$\varepsilon = \frac{A-C}{2C}$ (P anisotropy parameter)

$\gamma = \frac{N-L}{2L}$ (S anisotropy parameter)

$\delta = \frac{F+2L-C}{C}$ (off-axis parameter; elliptical anisotropy if $\delta = \varepsilon$)

where ρ is density. The expression for δ is simplified to omit quadratic terms [*Helbig and Thomsen*, 2005]. The ellipticity parameter in terms of Thomsen parameters has the form

$$\eta_\kappa = \frac{1 - V_{S0}^2/V_{P0}^2 + \delta}{\sqrt{1 - V_{S0}^2/V_{P0}^2} \; \sqrt{1 - V_{S0}^2/V_{P0}^2 + 2\varepsilon}}.$$

The parameter η used in Raysum can be calculated from a combination of Love parameters and η_κ using the following:

$$\eta = \frac{\eta\kappa \sqrt{(A-L)} \sqrt{(C-L)}}{A - 2L}$$

where in terms of Raysum inputs ρ, Vp, Vs, AVp, and AVs,

$$A = \rho^* \left(\text{Vp} - \text{Vp}^* \, \text{AVp}/100\right)^2$$

$$C = \rho^* \left(\text{Vp} + \text{Vp}^* \, \text{AVp}/100\right)^2$$

$$L = \rho^* \left(\text{Vs} + \text{Vs}^* \, \text{AVs}/100\right)^2$$

and AVp and AVs are negative for slow-axis symmetry.

In addition, we provide conversions between Love and Backus parameters below for completeness and because some published expression have typographical errors.

Love parameters in terms of Backus parameters are as follows (in *Sherrington et al.* [2004], equation (A11) for N has a typographical error):

$$A = a - b + c$$

$$C = a + b + c$$

$$F = a - 3c - 2(d + e)$$

$$L = d + e$$

$$N = d - e$$

Backus parameters in terms of Love parameters are as follows (in *Soukup et al.* [2013], Table VI has a typographical error for *b*):

$$a = \frac{3(A+C) + 2(F+2L)}{8}$$

$$b = \frac{C-A}{2}$$

$$c = \frac{A+C - 2(F+2L)}{8}$$

$$d = \frac{L+N}{2}$$

$$e = \frac{L-N}{2}$$

References

Aki, K., and P. G. Richards (1980), *Quantitative Seismology, Theory and Methods*, 948 pp., W. H. Freeman.

Aleksandrov, K. S., and T. V. Ryzhova (1961a), The elastic properties of rock-forming minerals: Pyroxenes and amphiboles, *Bull. Acad. Sci. USSR Geophys. Ser.*, *9*, 1165–1168.

Aleksandrov, K. S., and T. V. Ryzhova (1961b), Elastic properties of rock-forming minerals. II. Layered silicates, *Bull. Acad. Sci. USSR Geophys. Ser.*, *9*, 1165–1168.

Anderson, D. L. (1961), Elastic wave propagation in layered anisotropic media, *J. Geophys. Res.*, *66*, 2953–2963.

Audet, P. (2015), Layered crustal anisotropy around the San Andreas fault near Parkfield, California, *J. Geophys. Res. Solid Earth*, *120*, 3527–3543, doi:10.1002/2014JB011821.

Babuska, V., and M. Cara (1991), *Seismic Anisotropy in the Earth*, 219 pp., Springer Science & Business Media.

Backus, G. E. (1965), Possible forms of seismic anisotropy of the uppermost mantle under oceans, *J. Geophys. Res.*, *70*, 3429–3439.

Barberini, V., L. Burlini, and A. Zappone (2007), Elastic properties, fabric and seismic anisotropy of amphibolites and their contribution to the lower crust reflectivity, *Tectonophysics*, *445*(3–4), 227–244.

Barruol, G., and H. Kern (1996), Seismic anisotropy and shear-wave splitting in lower-crustal and upper-mantle rocks from the Ivrea zone—Experimental and calculated data, *Phys. Earth Planet. Inter.*, *95*, 175–194.

Becker, T. W., S. Chevrot, V. Schulte-Pelkum, and D. K. Blackman (2006), Statistical properties of seismic anisotropy predicted by upper mantle geodynamic models, *J. Geophys. Res.*, *111*, B08309, doi:10.1029/2005JB004095.

Bianchi, I., G. Bokelmann, and K. Shiomi (2015), Crustal anisotropy across northern Japan from receiver functions, *J. Geophys. Res. Solid Earth*, *120*, 4998–5012, doi:10.1002/2014JB011681.

Birch, F. (1960), The velocity of compressional waves in rocks to 10 kilobars: 1, *J. Geophys. Res.*, *65*(4), 1083–1102.

Browaeys, J. T., and S. Chevrot (2004), Decomposition of the elastic tensor and geophysical applications, *Geophys. J. Int.*, *159*, 667–678.

Brownlee, S. J., B. R. Hacker, M. Salisbury, G. Seward, T. A. Little, S. L. Baldwin, and G. Abers (2011), Predicted velocity and density structure of the exhuming Papua New Guinea ultrahigh-pressure terrane, *J. Geophys. Res.*, *116*, B08206, doi:10.1029/2011JB008195.

Crampin, S. (1977), Seismic anisotropy—Summary, *J. Geophys.-Zeitschrift Fur Geophysik*, *43*(1–2), 499–501.

Crampin, S. (1981), A review of wave motion in anisotropic and cracked elastic-media, *Wave Motion*, *3*, 343–391.

Crampin, S. (1994), The fracture criticality of crustal rocks, *Geophys. J. Int.*, *118*, 428–438.

Erdman, M. E., B. R. Hacker, G. Zandt, and G. Seward (2013), Seismic anisotropy of the crust: Electron-backscatter diffraction measurements from the basin and range, *Geophys. J. Int.*, *195*(2), 1211–1229.

Farra, V., and L. Vinnik (2000), Upper mantle stratification by P and S receiver functions, *Geophys. J. Int.*, *141*(3), 699–712.

Frederiksen, A. W., and M. G. Bostock (2000), Modelling teleseismic waves in dipping anisotropic structures, *Geophys. J. Int.*, *141*(2), 401–412.

Frederiksen, A. W., H. Folsom, and G. Zandt (2003), Neighbourhood inversion of teleseismic Ps conversions for anisotropy and layer dip, *Geophys. J. Int.*, *155*, 200–212.

Godfrey, N. J., N. I. Christensen, and D. A. Okaya (2000), Anisotropy of schists: Contribution of crustal anisotropy to active source seismic experiments and shear wave splitting observations, *J. Geophys. Res.*, *105*(B12), 27,991–928,007.

Hacker, B. R., G. A. Abers, and S. M. Peacock (2003), Subduction factory 1. Theoretical mineralogy, densities, seismic wave speeds, and H_2O contents, *J. Geophys. Res.*, *108*(B1), 2029, doi:10.1029/2001JB001127.

Helbig, K., and L. Thomsen (2005), 75-plus years of anisotropy in exploration and reservoir seismics: A historical review of concepts and methods, *Geophysics*, *70*(6), 9ND–23ND.

Ji, S., T. Shao, K. Michibayashi, S. Oya, T. Satsukawa, Q. Wang, W. Zhao, and M. H. Salisbury (2015), Magnitude and symmetry of seismic anisotropy in mica- and amphibole-bearing metamorphic rocks and implications for tectonic interpretation of seismic data from the southeast Tibetan Plateau, *J. Geophys. Res. Solid Earth*, *120*, 6404–6430, doi:10.1002/2015JB012209.

Ji, S., T. Shao, K. Michibayashi, C. Long, Q. Wang, Y. Kondo, W. Zhao, H. Wang, and M. H. Salisbury (2013), A new calibration of seismic velocities, anisotropy, fabrics, and elastic moduli of amphibole-rich rocks, *J. Geophys. Res. Solid Earth*, *118*, 4699–4728, doi:10.1002/jgrb.50352.

Kawakatsu, H. (2016), A new fifth parameter for transverse isotropy, *Geophys. J. Int.*, *204*, 682–685.

Kawakatsu, H., J.-P. Montagner, and T. A. Song (2015), *On DLA's n*, the Geologica Society of America.

Khazanehdari, J., E. H. Rutter, M. Casey, and L. Burlini (1998), The role of crystallographic fabric in the generation of seismic anisotropy and reflectivity of high strain zones in calcite rocks, *J. Struct. Geol.*, *20*(2–3), 293–299.

Kong, F., J. Wu, K. H. Liu, and S. S. Gao (2016), Crustal anisotropy and ductile flow beneath the eastern Tibetan Plateau and adjacent areas, *Earth Planet. Sci. Lett.*, *442*, 72–79.

Lakshtanov, D. L., S. V. Sinogeikin, and J. D. Bass (2007), High-temperature phase transitions and elasticity of silica polymorphs, *Phys. Chem. Miner.*, *34*, 11–22.

Levin, V., and J. Park (1998), *P-SH* conversions in layered media with hexagonally symmetric anisotropy: A cookbook, *Pure Appl. Geophys.*, *151*(2–4), 669–697.

Levin, V., L. Margheriti, J. Park, and A. Amato (2002a), Anisotropic seismic structure of the lithosphere beneath the Adriatic coast of Italy constrained with mode-converted body waves, *Geophys. Res. Lett.*, *29*(22), 2058, doi:10.1029/2002GL015438.

Levin, V., J. Park, M. Brandon, J. Lees, V. Peyton, E. Gordeev, and A. Ozerov (2002b), Crust and upper mantle of Kamchatka from teleseismic receiver functions, *Tectonophysics*, *358*(1–4), 233–265.

Levin, V., S. Roecker, P. Graham, and A. Hosseini (2008), Seismic anisotropy indicators in western Tibet: Shear wave splitting and receiver function analysis, *Tectonophysics*, *462*(1–4), 99–108.

Licciardi, A., and N. P. Agostinetti (2016), A semi-automated method for the detection of seismic anisotropy at depth via receiver function analysis, *Geophys. J. Int.*, *205*(3), 1589–1612.

Lin, F.-C., and M. H. Ritzwoller (2011), Helmholtz surface wave tomography for isotopic and azimuthally anisotropic structure, *Geophys. J. Int.*, *186*, 1104–1120.

Lin, F.-C., and B. Schmandt (2014), Upper crustal azimuthal anisotropy across the contiguous U.S. determined by Rayleigh wave ellipticity, *Geophys. Res. Lett.*, *41*, 8301–8307, doi:10.1002/2014GL062362.

Liu, H., and F. Niu (2012), Estimating crustal seismic anisotropy with a joint analysis of radial and transverse receiver function data, *Geophys. J. Int.*, *188*, 144–164.

Liu, Z., and J. Park (2017), Seismic receiver function interpretation: *Ps* splitting or anisotropic underplating?, *Geophys. J. Int.*, *208*, 1332–1341.

Liu, Z., J. Park, and D. M. Rye (2015), Crustal anisotropy in northeastern Tibetan Plateau inferred from receiver functions: Rock textures caused by metamorphic fluids and lower crust flow?, *Tectonophysics*, *661*, 66–80.

Love, A. E. H. (1944), *A Treatise on the Mathematical Theory of Elasticity*, Dover, New York.

Mainprice, D. (1990), A FORTRAN program to calculate seismic anisotropy from the lattice preferred orientation of minerals, *Comput. Geosci.*, *16*(3), 385–393.

McNamara, D. E., and T. J. Owens (1993), Azimuthal shear wave velocity anisotropy in the Basin and Range Province using Moho *Ps* converted phases, *J. Geophys. Res.*, *98*(B7), 12,003–012,017.

Moschetti, M. P., M. H. Ritzwoller, F.-C. Lin, and Y. Yang (2010), Seismic evidence for widespread western-US deep-crustal deformation caused by extension, *Nature*, *464*(7290), 885–U884.

Nagaya, M., H. Oda, and T. Kamimoto (2011), Regional variation in shear-wave polarization anisotropy of the crust in southwest Japan as estimated by splitting analysis of *Ps*-converted waves on receiver functions, *Phys. Earth Planet. Inter.*, *187*, 56–65.

Nagaya, M., H. Oda, H. Akazawa, and M. Ishise (2008), Receiver functions of seismic waves in layered anisotropic media: Application to the estimate of seismic anisotropy, *Bull. Seismol. Soc. Am.*, *98*(6), 2990–3006.

Naus-Thijssen, F. M. J., A. J. Goupee, S. E. Johnson, and S. S. Vel (2011a), The influence of crenulation cleavage development on the bulk elastic and seismic properties of phyllosilicate-rich rocks, *Earth Planet. Sci. Lett.*, *311*, 212–224.

Naus-Thijssen, F. M. J., A. J. Goupee, S. S. Vel, and S. E. Johnson (2011b), The influence of microstructure on seismic wave speed anisotropy in the crust: Computational analysis of quartz-muscovite rocks, *Geophys. J. Int.*, *185*, 609–621.

Nishizawa, O. (1982), Seismic velocity anisotropy in a medium containing oriented cracks—Transversely isotropic case, *J. Phys. Earth*, *30*(4), 331–347.

Niu, X., D. Zhao, J. Li, and A. Ruan (2016), *P* wave azimuthal and radial anisotropy of the Hokkaido subduction zone, *J. Geophys. Res. Solid Earth*, *121*, 2636–2660, doi:10.1002/2015JB012651.

Okaya, D. A., S. E. Johnson, and S. S. Vel (2010), The role of geological structure in crustal seismic anisotropy: Identification and quantification of "structural anisotropy", *Eos, American Geophysical Union Fall Meeting 2010*, Abstract S13A-1957.

Olugboji, T. M., and J. Park (2016), Crustal anisotropy beneath Pacific Ocean—Islands from harmonic decomposition of receiver functions, *Geochem. Geophys. Geosyst.*, *17*, 810–832, doi:10.1002/2015GC006166.

Ozacar, A. A., and G. Zandt (2004), Crustal seismic anisotropy in central Tibet: Implications for deformational style and flow in the crust, *Geophys. Res. Lett.*, *31*, L23601, doi:10.1029/2004GL021096.

Ozacar, A. A., and G. Zandt (2009), Crustal structure and seismic anisotropy near the San Andreas fault at Parkfield, California, *Geophys. J. Int.*, *178*, 1098–1104.

Park, J. (1996), Surface waves in layered anisotropic structures, *Geophys. J. Int.*, *126*(1), 173–183.

Park, J. A., and V. Levin (2016), Anisotropic shear zones revealed by backazimuthal harmonics of teleseismic receiver functions, *Geophys. J. Int.*, *207*(2), 1216–1243.

Peng, X., and E. D. Humphreys (1997), Moho dip and crustal anisotropy in northwestern Nevada from teleseismic receiver functions, *Bull. Seismol. Soc. Am.*, *87*(3), 745–754.

Porter, R., G. Zandt, and N. McQuarrie (2011), Pervasive lower-crustal seismic anisotropy in Southern California: Evidence for underplated schists and active tectonics, *Lithosphere*, *3*(3), 201–220.

Rasolofosaon, P. N. J., W. Rabbel, S. Siegesmund, and A. Vollbrecht (2000), Characterization of crack distribution: Fabric analysis versus ultrasonic inversion, *Geophys. J. Int.*, *141*, 413–424.

Ruempker, G., A. Kaviani, and K. Latifi (2014), *Ps*-splitting analysis for multilayered anisotropic media by azimuthal stacking and layer stripping, *Geophys. J. Int.*, *199*(1), 146–163.

Ryzhova, T. V. (1964), Elastic properties of plagioclase, *Bull. Acad. Sci. USSR Geophys. Ser.*, *7*, 1049–1051.

Savage, M. K. (1999), Seismic anisotropy and mantle deformation: What have we learned from shear wave splitting?, *Rev. Geophys.*, *37*(1), 65–106.

Schulte-Pelkum, V., and K. Mahan (2014a), Imaging faults and shear zones using receiver functions, *Pure Appl. Geophys.*, *171*, 2967–2991.

Schulte-Pelkum, V., and K. Mahan (2014b), A method for mapping crustal deformation and anisotropy with receiver functions and first results from USArray, *Earth Planet. Sci. Lett.*, *402*, 221–233.

Shapiro, N. M., M. H. Ritzwoller, P. Molnar, and V. Levin (2004), Thinning and flow of Tibetan crust constrained by seismic anisotropy, *Science*, *305*(5681), 223–236.

Shen, X. Z., X. H. Yuan, and J. S. Ren (2015), Anisotropic low-velocity lower crust beneath the northeastern margin of Tibetan Plateau: Evidence for crustal channel flow, *Geochem. Geophys. Geosyst.*, *16*, 4223–4236, doi:10.1002/2015GC005952.

Sherrington, H. F., G. Zandt, and A. W. Frederiksen (2004), Crustal fabric in the Tibetan Plateau based on waveform inversions for seismic anisotropy parameters, *J. Geophys. Res.*, *109*, B02313, doi:10.1029/2002JB002345.

Silver, P. G., and W. W. Chan (1991), Shear wave splitting and subcontinental mantle deformation, *J. Geophys. Res.*, *96*(B10), 16,429–416,454.

Skemer, P., I. Katayama, Z. Jiang, and S. Karato (2005), The misorientation index: Development of a new method for calculating the strength of lattice-preferred orientation, *Tectonophysics*, *411*(1–4), 157–167.

Soukup, S., R. Odom, and J. Park (2013), Modal investigation of elastic anisotropy in shallow-water environments: Anisotropy beyond vertical transverse isotropy, *J. Acoust. Soc. Am.*, *134*(185), 185–206.

Sun, Y., F. Niu, H. Liu, Y. Chen, and J. Liu (2012), Crustal structure and deformation of the SE Tibetan Plateau revealed by receiver function data, *Earth Planet. Sci. Lett.*, *349-350*, 186–197.

Sun, Y., J. Liu, K. Zhou, B. Chen, and R. Guo (2015), Crustal structure and deformation under the Longmenshan and its surroundings revealed by receiver function data, *Phys. Earth Planet. Inter.*, *244*, 11–22.

Takanashi, M., O. Nishizawa, K. Kanagawa, and K. Yasunaga (2001), Laboratory measurements of elastic anisotropy parameters for the exposed crustal rocks from the Hikada Metamorphic Belt, Central Hokkaido, Japan, *Geophys. J. Int.*, *145*, 33–47.

Takeuchi, H., and M. Saito (1972), Seismic surface waves, in *Seismology: Surface Waves and Earth Oscillations*, edited by B. A. Bolt, pp. 217–295, Academic Press, New York.

Tanimoto, T., and L. Rivera (2008), The ZH ratio method for long-period seismic data: Sensitivity kernels and observational techniques, *Geophys. J. Int.*, *172*, 187–198.

Tatham, D. J., G. E. Lloyd, R. W. H. Butler, and M. Casey (2008), Amphibole and lower crustal seismic properties, *Earth Planet. Sci. Lett.*, *267*, 118–128.

Thomsen, L. (1986), Weak elastic anisotropy, *Geophysics*, *51*, 1954–1966.

Valcke, S. L. A., M. Casey, G. E. Lloyd, J.-M. Kendall, and Q. J. Fisher (2006), Lattice preferred orientation and seismic anisotropy in sedimentary rocks, *Geophys. J. Int.*, *166*(2), 652–666.

Vaughan, M. T., and S. Guggenheim (1986), Elasticity of muscovite and its relationship to crystal structure, *J. Geophys. Res.*, *91*(B5), 4657–4664.

Vel, S. S., A. C. Cook, S. E. Johnson, and C. Gerbi (2016), Computational homogenization and micromechanical analysis of textured polycrystalline materials, *Comput. Methods Appl. Mech. Eng.*, *310*, 749–779.

Vergne, J., G. Wittlinger, V. Farra, and H. Su (2003), Evidence for upper crustal anisotropy in the Songpan-Ganze (northeastern Tibet) terrane, *Geophys. Res. Lett.*, *30*(11), 1552, doi:10.1029/2002GL016847.

Wang, Q., F. Niu, Y. Gao, and Y. Chen (2016), Crustal structure and deformation beneath the NE margin of the Tibetan Plateau constrained by teleseismic receiver function data, *Geophys. J. Int.*, *204*, 167–179.

Ward, D., K. Mahan, and V. Schulte-Pelkum (2012), Roles of quartz and mica in seismic anisotropy of mylonites, *Geophys. J. Int.*, *190*, 1123–1134.

Weiss, T., S. Siegesmund, W. Rabbel, T. Bohlen, and M. Pohl (1999), Seismic velocities and anisotropy of the lower continental crust: A review, *Pure Appl. Geophys.*, *156*, 97–112.

Wessel, P., W. H. F. Smith, R. Scharroo, J. F. Luis, and F. Wobbe (2013), Generic Mapping Tools: Improved version released, *Eos*, *94*, 409–410.

Xie, J., M. H. Ritzwoller, W. Shen, Y. Yang, and Y. Zheng (2013), Crustal radial anisotropy across eastern Tibet and the western Yangtze craton, *J. Geophys. Res. Solid Earth*, *118*, 4226–4252, doi:10.1002/jgrb.50296.

Xie, J. Y., M. H. Ritzwoller, S. J. Brownlee, and B. R. Hacker (2015), Inferring the oriented elastic tensor from surface wave observations: Preliminary application across the western United States, *Geophys. J. Int.*, *201*(2), 996–1021.

Zandt, G., M. Leidig, J. Chmielowski, D. Baumont, and X. H. Yuan (2003), Seismic detection and characterization of the Altiplano-Puna Magma body, central Andes, *Pure Appl. Geophys.*, *160*(3–4), 789–807.